Ofioliti An International Journal on Ophiolites and Modern Oceanic Lithosphere

JOURNAL PRE-PROOF

THE DISCOVERY AND GEOLOGICAL SIGNIFICANCE OF MIDDLE TRIASSIC SHAMA GABBRO IN THE ZHONGZA BLOCK, CHINA

To appear in OFIOLITI 52, 1 (2027)
DOI: https://doi.org/10.4454/ofioliti.v52i1.595

Received date: 28 April, 2026
Accepted date: 30 August, 2026
First published online 2 September, 2026

THE DISCOVERY AND GEOLOGICAL SIGNIFICANCE OF MIDDLE TRIASSIC SHAMA GABBRO IN THE ZHONGZA BLOCK, CHINA

Wenjing Yang*, Tianshe Cheng**, Xuebin Zhang*, Xiangqian He***, Guoping Wang•, Zhihua Dong*, Xujiang Cheng*, Lijun Guo*, Hongsheng Gao*

* Tianjin Institute of Geological Survey, Tianjin 300191, China
** Cores and Samples Center of Natural Resources, China Geological Survey, Sanhe, Hebei 065201, China,
*** Mengzi Yizhi Mining Co., Ltd., Mengzi, Yunnan 661100, China,
• Zijin Mining Group Co. Ltd., Longyan, Fujian 364200, China

✉ Corresponding author, email: chengtianshe515@163.com (T.-S. Cheng)

ABSTRACT

The subduction polarity, precise collisional timing, and Late Paleozoic–Early Mesozoic tectonic evolution of the eastern Paleo-Tethyan Jinshajiang Ocean remain highly controversial, restricting our comprehensive understanding of the tectonic framework and crust-mantle interaction of the Zhongza Block. To resolve these key scientific issues, this study systematically investigates a newly discovered Middle Triassic gabbro pluton in the Shama area of Batang County, located in the central Zhongza Block, eastern Paleo-Tethyan tectonic domain, through whole-rock major and trace element geochemistry, Sr–Nd isotopic analysis, and zircon U–Pb–Hf isotope geochronology. Petrographic observations indicate that the Shama gabbro is mainly composed of plagioclase, diopside, amphibole, and minor K-feldspar. Geochemically, the samples are characterized by low SiO_2 (45.2 wt.%–45.9 wt.%) and high MgO (8.24 wt.%–9.33 wt.%) contents, belonging to the tholeiitic series with insignificant Eu and Ce anomalies. These gabbros are enriched in large-ion lithophile elements (Rb, Th, U, Pb) and exhibit no obvious depletion of high-field-strength elements (Ta, Nb, Ti). The whole-rock initial $^{87}Sr/^{86}Sr$ ratios range from 0.708700 to 0.709559, with homogeneous negative $\varepsilon_{Nd}(t)$ values (−4.30 to −4.24) and two-stage Nd model ages (t_{DM2}(Nd)) of 1.36 Ga. Zircon $\varepsilon_{Hf}(t)$ values vary from −0.46 to 2.81, yielding two-stage Hf model ages (t_{DM2}(Hf)) of 945–1124 Ma. These isotopic features demonstrate that the parental magma originated from partial melting of depleted lithospheric mantle and experienced variable contamination by Mesoproterozoic ancient crustal materials. Zircon U–Pb dating defines a robust Middle Triassic formation age of 245 ± 1 Ma for the Shama gabbro. Integrated geochemical and regional geological evidence constrains a post-orogenic extensional tectonic setting for the pluton, indicating that the arc-continent collision between the Jinshajiang oceanic plate and the western Zhongza Block was completed before the Early–Middle Triassic, rather than occurring synchronously. The widespread Early–Middle Triassic intracontinental extension of the Zhongza Block is genetically linked to the back-arc spreading of the southern Cimmerian Continent and the initial opening of the Neo-Tethyan Ocean during the Permian, which corresponds to the global mantle dynamic evolution associated with Pangea breakup. This study provides new precise geochronological and geochemical constraints on the subduction-collision process of the Jinshajiang Ocean and the Mesozoic tectonic evolution of the eastern Paleo-Tethys, and further clarifies the regional geodynamic response to Neo-Tethys initiation.

Keywords: *Paleo-Tethyan tectonic domain, Sanjiang Orogenic Belt, Zhongza Block, Jinshajiang Suture Zone, Shama gabbro, Sr-Nd-Hf isotopes, Middle Triassic*

INTRODUCTION

Gabbro is a typical mantle-derived mafic intrusive rock, and its major-trace element and isotopic compositions can faithfully record magma source characteristics, crust-mantle interaction processes, and tectonic backgrounds of magmatic emplacement. Therefore, mafic intrusions are widely regarded as critical petrological probes for reconstructing regional tectonic-magmatic evolution (Wilson, 1989; Lu *et al*., 2002; Deng *et al*., 2004). The eastern Tethyan domain, especially the Sanjiang Orogen, preserves superimposed records of Paleo-Tethys closure, Neo-Tethys initiation, and multi-stage block collision and accretion, representing a key region for investigating the tectonic transition from Paleo-Tethys to Neo-Tethys regimes (Li *et al*., 2006; Pan *et al*., 2009; Metcalfe, 2013). The Middle Triassic is widely recognized as a pivotal tectonic transition period in East Tethys, during which the final closure of the Paleo-Tethys Ocean was synchronized with the initial spreading of the Neo-Tethys Ocean, accompanied by intensive regional magmatism and block amalgamation (Zhong *et al*., 1996; Wang *et al*., 2007).

As the core tectonic unit of the northern Sanjiang Orogen, the Zhongza Block is sandwiched between the Jinshajiang and Garzê-Litang suture zones and plays a decisive role in constraining the Paleo-Tethys oceanic subduction polarity, collision timing, and regional tectonic framework (Fig. 1) (Hou *et al*., 2003; Li *et al*., 2003; Zhang *et al*., 2008). Although previous studies have confirmed its affinity with the Yangtze Block and recognized multi-stage arc magmatism around the block, two core scientific controversies remain unresolved: (1) the precise timing and geodynamic nature of the transition from subduction-collision to post-orogenic extension along the western Zhongza Block; and (2) the regional tectonic response of the eastern Paleo-Tethys to the global Pangea breakup and initial Neo-Tethys opening during the Mesozoic.These long-standing debates severely restrict our comprehensive understanding of the Middle Triassic tectonic regime transition of the eastern Tethys.

The newly discovered Shama gabbro in the central Zhongza Block is the first systematically reported mafic intrusive body in this terrane. It features fresh exposure, homogeneous lithology, and weak late alteration, well preserving primary magmatic geochemical and isotopic signals. Therefore, this intrusion provides an ideal and previously missing petrological window to resolve the above tectonic controversies. Nevertheless, systematic geochronology, geochemistry, and isotopic constraints for the Shama gabbro are still blank, leaving its formation age, magma source, petrogenesis, and tectonic implication poorly understood. Accordingly, this study conducts integrated zircon U-Pb geochronology, zircon Hf isotopes, whole-rock major and trace element geochemistry, and Sr-Nd isotopic analyses on the Shama gabbro. We aim to solve four focused scientific questions: (1) to precisely constrain the Middle Triassic formation age of the Shama gabbro and establish its temporal position in the regional magmatic evolution; (2) to clarify the nature of the mantle source, melting characteristics, and crustal contamination process of the parental magma; (3) to determine the precise tectonic setting of the Shama gabbro and further constrain the Early-Middle Triassic tectonic transformation process of the western Zhongza Block; and (4) to link the local post-orogenic extensional magmatism to the global Mesozoic mantle dynamic event related to Pangea breakup and Neo-Tethys opening, thereby revealing the regional geodynamic response of the eastern Paleo-Tethys to global tectonic evolution.This work provides new key constraints for understanding the crust-mantle interaction, tectonic transition, and Paleo- to Neo-Tethys evolution of the eastern Tethyan domain.

REGIONAL GEOLOGICAL BACKGROUND AND PETROLOGICAL CHARACTERISTICS

The Shama gabbro intrudes the central part of the Zhongza Block. This block lies in the northern segment of the Sanjiang Orogenic Belt, on the eastern margin of the Qinghai-Tibet Plateau (Fig. 1a). Tectonically, the Shama gabbro lies within the core evolutionary zone of the eastern Tethyan tectonic domain. It occupies a tectonic-transition zone bounded by the Jinshajiang Suture Zone and the Ganzi-Litang Suture Zone (Fig. 1b). Its magmatic formation was strictly controlled by the regional tectonic dynamic regime, which was governed by multistage Paleo-Tethys Ocean evolution and inter-block collision and amalgamation (Pan *et al*., 2009; Metcalfe, 2013). The Shama gabbro occurs along north-northwest-trending faults, showing moderate outcrop extent, fresh exposures and homogeneous lithology. It has not experienced significant late-stage metamorphism and tectonic overprinting, and therefore well preserves magmatic-stage mineral assemblages and primary geochemical signatures (Zhang *et al*., 2008).

Regional stratigraphic units are well exposed (Fig. 2). The eastern area is dominated by the Late Permian Gangdagai Formation-Early Triassic Dang'en Formation. These units comprise back-arc foreland-basin clastic rocks interbedded with low-K basalts, which record the extensional tectono-magmatic response during block rifting (Zhang *et al*., 2008); The western part extensively exposes the Late Silurian Yongren Formation, Middle Devonian Gerong Formation, Qujing Formation, and Cangna Formation. These units form a succession of thick-bedded, stable carbonate-platform-facies limestones. Magmatic activity reached its climax during the Indosinian orogeny. Magmatic belts including the Early Permian-Middle Triassic Jomda-Weixi continental-marginal arc and the Late Triassic Yidun continental-marginal arc occur around the Zhongza Block. These belts preserve the complete evolutionary record of Paleo-Tethys Ocean subduction and closure (Zhu *et al*., 2009). Recognized magmatic rocks within this block are predominantly granitic intrusions with magmatic crystallization ages of 218–227 Ma. These are high-K calc-alkaline I-type granites generated within a subduction-arc tectonic setting. The genesis of these granites is closely linked to crust-mantle interaction driven by subduction and closure of the Jinshajiang Ocean and the Ganzi-Litang Ocean (Zhu *et al*., 2009). The Shama gabbro represents one of the rare mafic intrusive bodies in this region (Fig. 3a-c).

SAMPLING AND ANALYTICAL METHODS

Sampling

Fourteen samples were obtained from fresh exposures of the Shama gabbro for petrological, geochemical, and geochronological investigations. Ten samples (S01–S10) were chosen for petrological and whole-rock geochemical analyses; one sample (U01) for zircon U-Pb geochronology and in-situ Hf-isotope analyses; and three samples (A01–A03) for whole-rock Sr-Nd isotopic analyses. Sampling locations are presented in Fig. 2.

Analytical Techniques

Modal mineral abundance analysis

Modal mineral abundance analysis were conducted at the laboratory of the Regional Geological and Mineral Survey and Research Institute of Hebei Province. Modal mineral abundances of the Shama gabbro were obtained by point-counting on representative thin sections using an Olympus BX53-P petrographic microscope (Olympus Corporation, Tokyo, Japan) under transmitted-light optical microscopy (Chayes, 1956). A regular grid-based point-counting strategy was adopted to avoid subjective selection of mineral grains. A minimum of 800 points were counted for each thin section. The volumetric proportion (vol.%) of each mineral phase was calculated as the ratio of counted points for a given mineral to the total number of counted points. These values represent the modal volumetric mineral contents of the rock.

LA-ICP-MS Zircon U-Pb Isotope Analyses

Zircon grains were separated from rock samples using conventional mineral separation techniques, with assistance from the Hebei Provincial Institute of Regional Geology and Mineral Investigation. Cathodoluminescence (CL) images were obtained using a scanning electron microscope at the Institute of Geology and Geophysics, Chinese Academy of Sciences. Zircon U-Pb isotopic dating was performed by LA-ICP-MS at Wuhan Sample Solution Analytical Technology Co., Ltd. (Russell et al. 1978; Zhang et al. 2020; Baker et al. 2004; Hu et al. 2004; Hu et al. 2015; Woodhead et al. 2004; Fisher et al. 2014; Blichert-Toft et al. 1997). A UP193FX 193 nm ArF excimer laser ablation system (NewWave, Washington, USA) coupled with an Agilent 7500a ICP-MS instrument was used. The laser operated at a wavelength of 193 nm with a pulse width of <4 ns, and a laser spot diameter of 35 μm was adopted for analysis. External standardization was carried out using the international reference standards Plesovice zircon (weighted mean $^{206}Pb/^{238}U$ age = 337.13 ± 0.37 Ma) and Qinghu zircon (weighted mean $^{206}Pb/^{238}U$ age = 159.45 ± 0.16 Ma). Silicon (^{29}Si) from NIST SRM 612 glass was used as the internal standard. Isotopic ratios and elemental concentrations were processed using the GLITTER ver. 4.0 software (Macquarie University). Common Pb correction was applied using the Andersen ComPbCorr#3.17 program (Andersen et al. 2002). U-Pb concordia diagrams, age probability spectra, and weighted mean ages were calculated using Isoplot/Ex ver. 3.0 (Ludwig, 2003). Detailed analytical procedures and data processing are described in Liu et al. (2008, 2010a, 2010b).

In situ Zircon Hf Isotope Analysis

In situ zircon Hf isotope analyses were conducted using a Neptune Plus MC-ICP-MS (Thermo Fisher Scientific, Bremen, Germany) coupled with a Geolas HD ArF excimer laser ablation system (Coherent, Göttingen, Germany) at Wuhan Sample Solution Analytical Technology Co., Ltd., Hubei, China. All analyses were performed in single-spot ablation mode with a spot size of 44 μm. Detailed operating conditions and analytical methods follow those described by Hu et al. (2012, 2015).

Whole-rock Sr and Nd Isotope Analysis

Whole-rock Sr and Nd isotope analyses were conducted at Wuhan Sample Solution Analytical Technology Co., Ltd., Hubei, China. Sr and Nd isotope ratios were measured using a Neptune Plus MC-ICP-MS (Thermo Fisher Scientific, Dreieich, Germany) equipped with seven fixed electron multiplier ICs and nine Faraday cups fitted with 10^{11} Ω resistors. USGS reference materials BCR-2 and RGM-2 were used. Analyses of the BCR-2 and RGM-2 standard solution yielded a $^{87}Sr/^{86}Sr$ ratio of 0.705012±22 (2SD, n = 63) and 0.704173±20 (2SD, n = 20), which is consistent within uncertainty with published values of (Zhang et al., 2020; Li et al., 2012). In addition, analyses of the USGS reference materials BCR-2 (basalt) and RGM-2 (rhyolite) yielded $^{143}Nd/^{144}Nd$ ratios of 0.512641±11 (2SD, n = 82) and 0.512804±12 (2SD, n = 80), respectively, which agree within uncertainty with published data (Wei et al., 2006; Li et al., 2012). All data reduction for MC-ICP-MS isotope analyses was performed using “Iso-Compass” software（Zhang et al., 2020).

RESULTS

Mineralogical Characteristics

Microscopically, the Shama gabbro exhibits a medium- to fine-grained gabbroic texture (Fig. 3d) and is mainly composed of plagioclase, K-feldspar, pyroxene, and amphibole. Plagioclase (53 vol.%) occurs as subhedral tabular to lath-shaped crystals with grain sizes of 0.2–2 mm (locally 2–3 mm), and typically develops distinct oscillatory zoning and polysynthetic twinning (Fig. 3e). Most plagioclase cores have undergone kaolinization and sericitization, with minor epidotization; individual grains display anti-rapakivi texture. K-feldspar (5 vol.%) occurs as anhedral interstitial perthite (0.2–1 mm) that encloses plagioclase grains and shows weak kaolinization. Pyroxene (20 vol.%) is predominantly diopside, forming subhedral prismatic grains of 0.1–2 mm (rarely 2–2.5 mm). Most pyroxene grains are rimmed by amphibole reaction coronas (Fig. 3f) and are partially replaced by uralite and chlorite along grain margins and cleavages, while relict pyroxene is locally preserved in grain cores. Amphibole (20 vol.%) occurs as subhedral prismatic to granular crystals ranging from 0.1 to 1.5 mm in size, partly forming reaction rims surrounding pyroxene, and is also variably altered to uralite and chlorite. Opaque minerals account for 2 vol.% of the rock, occurring as subhedral to anhedral grains with sizes of 0.2–0.5 mm (locally 0.01–0.2 mm). Minor accessory minerals include apatite and zircon. Secondary alteration minerals mainly consist of kaolinite, sericite, zoisite, uralite, and chlorite.

Zircon U–Pb Geochronology

Cathodoluminescence (CL) images of individual zircon grains (Fig. 4a) reveal that zircons separated from the Shama gabbro display well-developed, intact crystal morphologies. Most grains exhibit a long prismatic habit, with subordinate irregular granular grains, grain lengths of 60–180 μm, and length-width ratios of 1.4–2.8. These zircons show clear oscillatory zoning, with no metamorphic overgrowth rims or inherited residual cores. Their Th/U ratios vary from 0.14 to 1.32, yielding an average value of 0.51. As proposed by Wu *et al*. (2004), magmatic zircons are generally characterized by elevated Th and U contents and high Th/U ratios (typically > 0.4). Accordingly, the zircon grains from the Shama gabbro are consistent with typical magmatic zircon signatures. The zircon U-Pb isotopic dating data of the Shama gabbro are listed in Table 1. In the U-Pb concordia diagram(Fig. 4b), all data points plot on or near the concordia line. The weighted mean ^{206}Pb/^{238}U age is 245 ± 1 Ma (MSWD = 1.4; n = 30), which represents the formation age of the Shama gabbro.

Zircon In Situ Hf Isotope

Zircon in-situ Hf isotope analysis was conducted on the Shama gabbro, yielding 30 valid analytical data points (Table 2). The results show that the ^{176}Hf/^{177}Hf ratios of the zircons range from 0.282608 to 0.282708, with an average of 0.282665±0.000024, which is slightly higher than the average value of the depleted lithospheric mantle at the corresponding age (^{176}Hf/^{177}Hf ≈ 0.282600; Zindler *et al*., 1986), indicating a potential lithospheric mantle-derived component in the magma source. The ε_{Hf}(t) values of the zircons are predominantly positive, ranging from −0.46 to 2.81 with an average of 0.82±0.80. Most ε_{Hf}(t) values (27 out of 30) fall within the range of 0–3 (Fig. 5a), which is characteristic of magmas derived from the partial melting of a depleted lithospheric mantle or a mantle source slightly modified by crustal material (Fig. 5b) (Gao *et al*., 2008). The small number of slightly negative ε_{Hf}(t) values (−0.46 to −0.01) may result from minor contamination by ancient crustal materials during magma ascent, but this contamination is limited given the overall positive ε_{Hf}(t) trend. The two-stage model ages (t_{DM2}) of the zircons range from 945 to 1124 Ma with an average of 1050 ± 42.6 Ma, corresponding to the Mesoproterozoic. This age range is consistent with the formation age of the lithospheric mantle in the study area, as constrained by regional mantle xenolith studies (Liu *et al*., 2012), suggesting that the magma was derived from the partial melting of Mesoproterozoic lithospheric mantle rather than a juvenile mantle source. The $f_{Lu/Hf}$ values of the zircons range from −0.96 to −0.91 with an average of −0.94 ± 0.01, which is close to −1. This indicates that zircon has not experienced significant Hf isotope re-equilibration with the surrounding matrix since its crystallization (Amelin *et al*., 2000), confirming that the measured Hf isotopic compositions can reliably reflect the isotopic characteristics of the magma during its formation.

Integrated with previous petrological and geochemical results, the positive ε_{Hf}(t) values and relatively high ^{176}Hf/^{177}Hf ratios of the Shama gabbro indicate that its parental magma was predominantly derived from partial melting of depleted lithospheric mantle. The sporadic slightly negative ε_{Hf}(t) values can be explained by limited crustal assimilation during magma emplacement, rather than substantial crustal contamination within the mantle source (Pearce, 2008). This petrogenetic scenario matches the Late Permian–Early Triassic tectonic framework of the study area, where post-subduction extensional conditions prevailed and facilitated the upwelling and partial melting of lithospheric mantle materials (Chen *et al*., 2020).

Whole-Rock Geochemistry

Major and trace element compositions, CIPW normative mineral abundances, and representative geochemical ratios of the Shama gabbro are presented in Table 3.

Major Elements

The Shama gabbro is characterized by mafic major-element compositions typical of gabbroic rocks (Fig. 6a) (Middlemost, 1994). SiO_2 contents range from 45.2 wt. % to 45.9 wt. %, with a mean of 45.4 wt. t%. Total iron (FeO^T) averages 12.0 wt. %, MgO averages 8.71 wt. %, and the corresponding $Mg^{\#}$ (magnesium number) is 54.7, indicating a mafic igneous rock derived from a mantle-derived magma with relatively primitive geochemical affinities. Major rock-forming elements are uniform: Al_2O_3 = 14.8 wt. %, CaO = 9.59 wt. %, Na_2O = 1.96 wt. %, and K_2O = 0.62 wt. %. The Na_2O/K_2O ratio averages 3.16, suggesting a weak sodic affinity. TiO_2 is low and consistent (mean = 1.50 wt. %), and P_2O_5 averages 0.23 wt. %, both lower than average mid-ocean ridge basalt (MORB), implying a mantle source that underwent a certain degree of partial melting or early fractional crystallization. Geochemical classification indices reveal a low degree of magmatic differentiation: the differentiation index (DI) averages 21.2, far below values for intermediate and felsic rocks, confirming an early stage of magmatic evolution. Both A/MF (0.62 ± 0.06) and C/MF (0.73 ± 0.05) are less than 1, supporting a tholeiitic magmatic origin (Fig. 6b) (Irvine *et al.,* 1971). CIPW normative mineral calculations show a dominant mafic mineral assemblage: olivine (16.1 wt. %), diopside (13.9 wt. %), and hypersthene (13.2 wt. %), with total mafic minerals reaching 43.2 wt. %, typical of mafic intrusive rocks. Accessory phases are dominated by ilmenite (3.01 wt. %) and magnetite (2.22 wt. %), with low apatite (0.55 wt. %), consistent with the low TiO_2 and P_2O_5 contents. Mafic minerals (especially olivine and hypersthene) show relatively large variations (coefficients of variation 19.1 wt. % and 28.7 wt. %, respectively), whereas plagioclase and diopside are more uniform (CV = 3.44 wt. % and 10.1 wt. %, respectively). This compositional scatter likely reflects early, discontinuous crystallization of olivine, indicating episodic changes in temperature and pressure within the magma chamber (Winter, 2014; Putirka, 2017).

Trace Elements

Analytical results for rare earth elements (REE) and trace elements from 10 samples of the Shama gabbro reveal typical geochemical affinities of mantle-derived mafic rocks, providing critical constraints on magma origin and tectonic setting. Total rare earth element contents (ΣREE) range from 55.9 to 122.4 ppm, with a mean of 93.0 ppm. The chondrite-normalized REE patterns show enrichment in light rare earth elements (LREEs) and relative depletion in heavy rare earth elements (HREEs): LREE = 69.7 ppm, HREE = 23.3 ppm, LREE/HREE = 2.97, and chondrite-normalized $(La/Yb)_N$ = 2.41. The patterns are smooth and right-sloping, without significant fractionation or "spikes" or "troughs" (Fig. 7a). No obvious Eu or Ce anomalies are observed: δEu = 0.98 (0.94–1.02) and δCe = 0.95 (0.89–0.97), indicating no significant accumulation or fractionation of plagioclase during crystallization, and no Ce mobility under oxidizing conditions or seawater alteration (Mc Donough *et al.,* 1995; Niu *et al.,* 2003).

In terms of trace element compositions (Fig. 7b), the Shama gabbro displays fractionated large ion lithophile elements (LILEs) and relatively stable high field strength elements (HFSEs). Sr contents

are high (Sr = 154.4 ppm), whereas Rb is low (Rb = 26.9 ppm), with a mean Rb/Sr ratio of 0.18. Zr contents are uniform (Zr = 113.4 ppm, CV = 3.53%), and Nb is low (Nb = 7.59 ppm). The Zr/Hf ratio averages 50.3, close to chondritic values. Among transition metals, Sc is high (44.0 ppm) and Y is moderate (33.0 ppm), with a mean Sc/Y ratio of 1.34. Key petrogenetic ratios include Nb/Ta = 15.7, Th/U = 4.76, and Zr/Nb = 15.2.
Integrated interpretations suggest that the Shama gabbro was generated by minor degrees of partial melting of a slightly depleted lherzolite mantle source. The magma underwent negligible fractional crystallization or crustal contamination during ascent. The pluton formed in a back-arc basin extensional setting associated with subduction, genetically linked to back-arc spreading and mantle partial melting triggered by plate subduction (Stern, 2002; Pearce, 2014).

Sr-Nd Isotopes
The whole-rock Sr–Nd isotopic ratios of the Shama gabbro were calculated based on the weighted mean age obtained for the samples. Whole-rock Sr–Nd isotopic compositions are listed in Table 4. The samples have Rb and Sr contents of 16.1×10^{-6}–35.4×10^{-6} and 146×10^{-6}–183×10^{-6}, respectively, with Rb/Sr ratios ranging from 0.11 to 0.19. Sm and Nd contents are 5.14×10^{-6}–5.92×10^{-6} and 19.7×10^{-6}–22.7×10^{-6}, respectively, with Sm/Nd ratios of 0.26–0.27. The samples yield initial $^{87}Sr/^{86}Sr$ ratios (($^{87}Sr/^{86}Sr)_i$) of 0.708700–0.709559, $^{143}Nd/^{144}Nd$ ratios of 0.512356–0.512361, and $^{147}Sm/^{144}Nd$ ratios of 0.1564–0.1614. The $\varepsilon_{Nd}(t)$ values range from −4.30 to −4.24, and the two-stage Nd isotopic model ages (t_{DM_2}) are 1360 Ma. Sr-Nd isotopic analyses of the samples indicate that the magma of the Shama gabbro was likely derived from ancient depleted lithospheric mantle, with minor crustal material incorporated during magma evolution (Fig. 8) (Bouvier A *et al*., 2008).

DISCUSSION

Intrusion Age

Previous studies have generally assigned the ultramafic-mafic magmatic rocks exposed within the Zhongza Block to Indosinian magmatism (Sichuan Bureau of Geology, 1980), yet reliable high-precision chronological constraints are absent. The Zhongza Block lies between the Jinshajiang Suture Zone to the west and the Garzê-Litang Suture Zone to the east. Tectonically, it occupies the east-central segment of the Tethyan tectonic domain, rendering it a key locality for investigating the geological evolution of this domain. It is widely accepted that, from the late Early Permian through the Triassic, the western margin of the Zhongza Block experienced a tectonic transition from a passive continental margin to arc-continent collision, driven by subduction and consumption of the Jinshajiang oceanic plate (Wang *et al*., 2024); whereas the eastern margin of the Zhongza Block developed an active continental-margin and continental-margin-arc setting during the Late Triassic, as a consequence of subduction and consumption of the Garzê-Litang oceanic plate (Lu *et al*., 2022). In this study, we report the first discovery of the Shama gabbro and present high-precision geochronological data for this intrusion. Zircon U-Pb dating yields an age of 245 ± 1 Ma, constraining its formation to the Middle Triassic. The newly identified Middle Triassic gabbro provides the first robust evidence for distinct mafic magmatic intrusive activity within the Zhongza Block during the Middle Triassic, filling an important gap in our understanding of the block's magmatic evolution for this time interval.

As a key junction for the eastward extension of the Meso-Tethyan tectonic domain, the Zhongza Block records tectono-magmatic responses to the evolutionary history of the Meso-Tethys Ocean. The Middle Triassic represents a pivotal transitional interval, marking the shift from peak spreading to subduction-driven shrinkage of the Meso-Tethys Ocean. This interval also corresponds to progressive intensification of subduction of the Jinshajiang oceanic plate, a major branch of the

Meso-Tethys Ocean (Wang *et al*., 2024). Magmatic records of this interval remain relatively scarce within the eastern-extending segment of the Tethyan tectonic domain in the Hengduan Mountains. This scarcity has fueled ongoing debates regarding the spatiotemporal framework for the middle-stage spreading and subduction of the Meso-Tethys Ocean. The newly documented Middle Triassic gabbro provides invaluable magmatic evidence for understanding the middle-stage evolution of the Meso-Tethys Ocean. Its genesis is broadly consistent with tectonic events recorded by coeval eclogites within the eastern Jinshajiang Suture Zone (Li *et al*., 2025), collectively constraining the tectonic evolutionary features of the eastern extension of the Tethyan domain during the Middle Triassic. Precise determination of the gabbro's formation age enables us to establish spatiotemporal links between this intrusion and key middle-stage tectonic events of the Meso-Tethys Ocean, including intensified subduction of the Jinshajiang oceanic plate and peak spreading of the Garzê-Litang Ocean; its petrogeochemical and isotopic signatures can trace mantle source compositions, slab-subduction intensity, and fluid-metasomatism processes during the middle-stage evolution of the Meso-Tethys Ocean. This fills the gap in Middle-Triassic magmatic records for the eastern extension of the Tethyan tectonic domain, and is consistent with published findings for Late Permian-to-Middle Triassic island-arc magmatism along the Jinshajiang tectonic belt (Wang *et al*., 2024). Meanwhile, comparative investigations between this gabbro and coeval magmatic rocks from adjacent terranes (the Songpan-Garzê Terrane) (Lu *et al*., 2022) can further refine regional constraints on the eastward evolution of the Meso-Tethys Ocean. These comparisons furnish critical support for resolving ongoing debates concerning the timing of middle-stage spreading and subduction of the Meso-Tethys Ocean, and offer new magmatic constraints for deciphering the multi-terrane accretion mechanism of the Paleo-Tethyan system along the southeastern margin of the Qinghai-Tibet Plateau.

Petrogenesis of the Shama Gabbro

Alteration, Fractional Crystallization and Crustal Contamination

Major element analyses of 10 samples from the Shama gabbro show that their SiO_2 contents range from 45.2 wt. % to 45.9 wt. % (average 45.4 wt. %), which is consistent with the geochemical classification of gabbro proposed by the International Union of Geological Sciences (IUGS) (Le Maitre, 2002). The $Mg^{\#}$ values vary from 52.4 to 56.8 (average 54.7), displaying an overall low $Mg^{\#}$ signature, indicating that the magma underwent a certain degree of crystal fractionation. Primitive mantle-derived magmas generally have $Mg^{\#}$ values greater than 60, and low $Mg^{\#}$ values are a typical indicator of mineral fractional crystallization (Wilson, 1989).

The coupled relationship between approximate loss-on-ignition (LOI, average 3.02%) and Fe^{3+}/Fe^{2+} ratios (0.003 – 0.238, average 0.137) shows that all samples have LOI values clustering within the range of 2.32 wt. % – 3.68 wt. %, with overall low Fe^{3+}/Fe^{2+} ratios. Combined with the stable K_2O contents (0.52 wt. % – 0.68 wt. %, average 0.62 wt. %), these features indicate that the rocks experienced weak to moderate hydrothermal alteration. LOI values are below the 5 wt. % threshold for strong alteration, suggesting that this process was dominated by low-temperature hydration under reducing conditions. The absence of anomalous K_2O enrichment excludes late-stage potassic fluid metasomatism (Humphris et al., 1995). Nb, Ta, Sr, Rb, Hf, Zr, La, Eu, and K_2O for all samples exhibit low correlations with LOI (Fig. 9), indicating that alteration has a limited effect on the elemental compositions of the Shama gabbro.

The crystal fractionation process is constrained by multi-dimensional diagrams. Plagioclase has An values ranging from 61.8% to 65.1% (average 63.0%) (CIPW theoretical calculation values) (Table 3), belonging to the labradorite series (An 50–70). This An range corresponds to a medium- to high-pressure crystallization environment at depths of 10–35 km (Tatsumi et al., 1995). When subdivided into two subgroups, divergent geochemical trends are revealed in the Harker diagrams (Fig. 10). Six samples (S01, S02, S06, S08, S09, S10) show a strong $Mg^{\#}$-SiO_2 correlation

(R^2=0.7655), consistent with fractional crystallization dominated by olivine and clinopyroxene, while their CaO-SiO_2 correlation is poor (R^2=0.2728), precluding extensive early plagioclase fractionation (O' Hara, 1968). The remaining four samples (S03, S04, S05, S07) deviate from this primary trend, with negligible $Mg^{\#}$-SiO_2 correlation (R^2=0.0551) but prominent CaO-SiO_2 correlation (R^2=0.7114). These features indicate that samples S03-S04-S05-S07 may have been modified by limited crustal assimilation. Collectively, the magma underwent moderate crystal fractionation coupled with minor crustal contamination in a deep magma chamber.

Mantle-derived magmatic rocks that have experienced crustal contamination commonly display pronounced negative Nb-Ta, Zr-Hf, and Ti anomalies, with La/Sm ratios greater than 5 (Wood DA et al., 1980). Most samples from the Shama gabbro lack prominent negative Nb-Ta, Zr-Hf, and Ti anomalies and yield La/Sm ratios lower than 5, whereas only a small subset of samples (S04, S05, S06) display weak negative Nb-Ta anomalies. On the $(La/Nb)_{PM}$–$(Th/Nb)_{PM}$ diagram (Fig. 11a) and $(Th/Yb)_{PM}$–Nb/La diagram (Fig. 11b), all analyzed samples fall within the crustal-contamination field. Moreover, mantle-derived magmas subjected to substantial crustal contamination typically yield $(Th/Nb)_{PM}$ ratios greater than 1 and Nb/La ratios lower than 1. The gabbro samples from this study yield $(Th/Nb)_{PM}$ values of 4.14–7.09 and Nb/La values of 0.35–0.89, consistent with signatures of crustal contamination (Neal CR et al., 2002). Collectively, these observations indicate that the Shama gabbro experienced crustal assimilation.

Petrogenesis and Tectonic Setting

Three whole-rock samples of the Shama gabbro exhibit initial $(^{87}Sr/^{86}Sr)_i$ values ranging from 0.708700 to 0.709559 (mean = 0.709168), which are slightly higher than that of the mantle endmember (CHUR = 0.7045) (Bouvier A et al., 2008). The $\varepsilon_{Nd}(t)$ values vary from -4.29 to -4.24 (mean = -4.26), showing weak negative characteristics. Notably, the sample points plot far from the continental crust endmember ($\varepsilon_{Nd}(t) \approx -10$), indicating slight crustal contamination (Bouvier A et al., 2008).

In Fig. 5a, 30 zircon analysis points yield $\varepsilon_{Hf}(t)$ values of -0.46 to 2.81 (mean = 0.82 ± 0.80), which are close to the mantle endmember (CHUR = 0) with a slight positive deviation. A histogram reveals a unimodal distribution of $\varepsilon_{Hf}(t)$, suggesting that the zircons crystallized in a relatively homogeneous magmatic system (Zindler et al., 1986).

The Nd-Hf isotope coupling relationship gives $\Delta\varepsilon_{Hf}$ = 3.73 ($\Delta\varepsilon_{Hf} = \Delta\varepsilon_{Hf}(t) - 1.53 \times \varepsilon_{Nd}(t) - 3.6$; Vervoort et al., 1999). The significantly positive $\Delta\varepsilon_{Hf}$ value indicates that the magmatic source region contains an ancient depleted lithospheric mantle component. Combined with the two-stage model ages ($t_{DM2}(Nd)$ = 1.36 Ga, $t_{DM2}(Hf)$ = 1050 Ma), qualitative geochemical evidence suggests limited crustal contamination, with small amounts of Mesoproterozoic juvenile crustal material potentially incorporated during magma ascent. These model ages are consistent with the formation age of the regional Mesoproterozoic basement crust (Hu et al., 2018). Furthermore, the $\varepsilon_{Nd}(t)$ values only fluctuate by 0.05, indicating that the contamination process occurred at the magma chamber stage with a uniform degree of contamination.

In summary, the petrogenetic process of the Shama gabbro can be summarized as follows: partial melting of the depleted mantle formed the primitive magma → moderate fractional crystallization of olivine + clinopyroxene occurred in a deep magma chamber under medium-high pressure conditions → a small amount of Mesoproterozoic juvenile crustal material was incorporated → shallow emplacement and cooling → weak to moderate hydrothermal alteration in the later stage. Overall, it retains the main geochemical characteristics of the mantle source region, providing important constraints for the study of Middle Triassic magmatism and crust-mantle interaction in the region (Li et al., 2020).

On the 2Nb-Zr/4-Y (Fig. 12a) and Hf/3-Th-Nb/16 (Fig. 12b) diagrams, the samples plot in the field of island-arc tholeiitic basalts; whereas on the TiO_2 vs. Zr (Fig. 12c) and Zr/Y vs. Zr (Fig. 12d) diagrams, the samples are mainly distributed in the intraplate basalt field, with some samples overlapping the mid-ocean ridge basalt field. This combined characteristic indicates that the Shama gabbro formed in an intraplate extensional environment during the Middle Triassic, rather than a typical island-arc or mid-ocean ridge environment (Taylor SR et al., 1985; Mcdonough WF et al., 1996; Meschede M et al., 1986; Steiger RH et al., 1977; Winchester JA et al., 1977). This finding suggests that the Zhongza block was in a post-orogenic extensional stage during the Middle Triassic, further constraining the timing of the transition from compression to extension in the Zhongza block and clarifying the tectonic setting of the Zhongza block during the Middle Triassic.

Geological Significance

The Zhongza Block occupies the central segment of the Sanjiang Orogen within the southwestern Eastern Tethyan tectonic domain. Its eastern margin hosts the Yidun Magmatic Arc; the block is bounded by the Garzê-Litang Suture Zone and the Yangtze Plate to the east, and by the Jinshajiang Suture Zone to the west. This distinctive tectonic setting renders the geological evolution of the Zhongza Block highly significant for deciphering geodynamic processes of the eastern Paleo-Tethyan Orogen (Fu *et al*., 2024; Van *et al*., 2011; Yang *et al*., 2015). Multiple lines of previous evidence indicate that the Zhongza Block constituted an integral segment of the western Yangtze Block margin during the Late Paleozoic (Zhu *et al*., 2008; Zhou *et al*., 2018; Zeng *et al*., 2019). During the Late Permian-Late Triassic, rifting of the Zhongza Block away from the western margin of the Yangtze Plate occurred in response to spreading of the Garzê-Litang Ocean (Wang *et al*., 2021). From the Early-Middle to Late Triassic, west-directed subduction of the Garzê-Litang oceanic plate beneath the Zhongza Block initiated, giving rise to the Yidun Magmatic Arc along its eastern margin, prior to final closure of the Garzê-Litang Ocean by the end of the Late Triassic. To the west of the Zhongza Block, the Jinshajiang oceanic basin opened from the Early Carboniferous to Early Permian and represents a major oceanic domain of the Paleo-Tethys. Oceanic subduction commenced during the Permian (Zhang *et al*., 2021). Arc-continental collisional orogeny occurred during the Early–Middle Triassic (Jian *et al*., 2009; Wang *et al*., 1999; Wang *et al*., 2021), with final closure of the oceanic basin achieved by the Middle Triassic (Pan *et al*., 2001; Zhu *et al*., 2020). Substantial debates still persist concerning the subduction polarity of the Permian Jinshajiang oceanic plate and the precise timing of arc-continent collisional orogeny (Wu *et al*., 2020; Meng *et al*., 2024; Chen *et al*., 2021; Shi *et al*., 2018). Accordingly, a unified evolutionary model for the eastern Paleo-Tethyan Orogen has not yet been achieved (Zindler *et al*., 1986; Yin *et al*., 2000; Zhang *et al*., 2023).

Widely exposed along the western margin of the Zhongza Block, the Permian Gangdagai Formation contains abundant amygdaloidal basalt, vesicular basalt, and basaltic volcanic breccia. Previous studies suggest that these basaltic lavas formed within an intracontinental extensional tectonic setting (Wang *et al*., 2022; Lü *et al*., 2012; Jia *et al*., 2020). In another investigation, we obtained a precise zircon U-Pb age of 250 ± 2 Ma for these basalts (unpublished data). Accordingly, the intracontinental-extensional basalts of the Gangdagai Formation were emplaced during the Early Triassic, instead of the Permian as previously interpreted.

The initial Sr isotopic ratios ($(^{87}Sr/^{86}Sr)_i$) of the Shama gabbro range from 0.708700 to 0.709559 (average = 0.709168), its $\varepsilon_{Nd}(t)$ values vary from −4.30 to −4.24 (average = −4.26), and $\Delta\varepsilon_{Hf}$ = 3.73 (Vervoort *et al*., 1999). The above geochemical characteristics indicate that the magma source was dominated by ancient depleted mantle, contaminated by minor amount of Mesoproterozoic juvenile crustal materials. The two-stage model ages of the pluton (t_{DM2}(Nd) = 1.36 Ga, t_{DM2}(Hf) = 1050 Ma) are consistent with the formation age of regional Mesoproterozoic basement crust (Hu *et al*., 2018). This confirms that the magmatism of the Shama gabbro is closely related to basement activation, and provides direct evidence and geochronological constraints for clarifying the internal linkage between basement activation and magmatism. Tectonic discrimination results (Fig. 11) show that the Shama gabbro formed in an intraplate extensional tectonic setting. Accordingly, we preliminarily propose that the western margin of the Zhongza Block was in an intracontinental extensional setting at least from the Early Triassic to the Middle Triassic, while its eastern margin was still in an arc-continental collisional tectonic setting related to the Garzê-Litang oceanic plate (Fig. 13). As stated previously, subduction and collision of the Garzê-Litang oceanic plate beneath the Zhongza Block initiated in the Early–Middle Late Triassic. Thus, the Early–Middle Triassic extensional setting of the Zhongza Block cannot be post-orogenic extension resulting from the Late Triassic collision between the Garzê-Litang oceanic plate and the Zhongza Block. In contrast, subduction of the Jinshajiang oceanic plate on the western side of the Zhongza Block took place in the Permian. We therefore preliminarily suggest that the Permian Jinshajiang oceanic plate underwent rapid eastward subduction beneath the Zhongza Block, and had entered the post-orogenic extensional tectonic environment by the Early–Middle Triassic. The timing of arc-continental collision between the Jinshajiang oceanic plate and the western margin of the Zhongza Block should be earlier than the Early–Middle Triassic, rather than during this period.

These findings furnish new constraints on Permian subduction polarity of the Jinshajiang oceanic plate and the exact timing of arc-continent collisional orogeny. Meanwhile, widespread Early-Middle-Triassic intracontinental extension along the western margin of the Zhongza Block may be linked to the onset of back-arc spreading within the southern segment of the Permian Cimmerian Continent and the opening of the Neo-Tethyan Ocean (Muttoni *et al*., 2009; Seton *et al*., 2012; Yoshida *et al*., 2014; Zindler *et al*., 1986; Vervoort *et al*., 1999).

CONCLUSION

(1) Zircon U–Pb precise dating yields a consistent Middle Triassic crystallization age of 241 Ma for the Shama gabbro. Combined with field geological observations and petrographic characteristics, this gabbro represents a newly identified mafic magmatic unit in the Zhongza Block, supplementing the magmatic records of the eastern Paleo-Tethyan tectonic domain.

(2) Whole-rock major, trace element, Sr–Nd isotopic, and zircon Hf isotopic data constrain the petrogenesis of the Shama gabbro. The samples exhibit uniform whole-rock $(^{87}Sr/^{86}Sr)_i$ of 0.708700–0.709559 and negative whole-rock εNd(t) values ranging from −4.30 to −4.24. Zircon grains yield variable $\varepsilon_{Hf(t)}$ values from −0.46 to 2.81, with two-stage Hf model ages (t_{DM2}) of 945–1124 Ma (average of 1050 ± 42.6 Ma), corresponding to the Mesoproterozoic. These systematic isotopic features demonstrate that the Shama gabbro originated from ancient Mesoproterozoic lithospheric mantle rather than juvenile mantle material. The magma underwent moderate fractional crystallization within a deep-seated magma chamber, accompanied by minor crustal assimilation during magma ascent.

(3) Comprehensive petrological and geochemical analyses suggest that the Shama gabbro formed in an intracontinental extensional setting during the Middle Triassic. The coupled Sr–Nd–Hf isotopic compositions and fractional crystallization characteristics record obvious crust–mantle interaction and lithospheric extension. This study provides precise geochronological and isotopic constraints for the tectonic transition and magmatic response of the eastern Paleo-Tethyan orogen

ACKNOWLEDGMENTS

We thank the editors and anonymous reviewers for their critical reviews and excellent suggestions that helped to improve this manuscript. We thank Xiaofei Zhang and Shuo Li for their help and valuable comments. We would like to express our gratitude to the leadership and staff of the Exploration Department at the Tianjin Geological Survey and Research Institute for their assistance and support with the field research.

Author Contributions: Conceptualization, T.C., and W.Y.; methodology, T.C. and W.Y.; software, T.C., W.Y., X.Z. and X.H.; validation, G.W. and X.C; formal analysis, L.G. and Z.D.; investigation, T.C., W.Y., H.G. and X.Z.; resources, T.C. and W.Y.; data curation, T.C., W.Y., X.Z. and X.H.; writing—original draft preparation, T.C. and W.Y.; writing—review and editing, G.W. and X.C.; visualization, T.C. and W.Y.; supervision, W.Y.; project administration, Z.D. and H.G.; funding acquisition, Z.D. and W.Y. All authors have read and agreed to the published version of the manuscript.

Funding: This research was funded by grants from China Geological Survey (Grants DD20242250, [2010]01–19–01).

Data Availability Statement: The authors confirm that the data generated or analyzed during this study are provided in full within the published article.

Conflicts of interest: All the authors declare that there is no conflict of interest regarding the publication of this article.

REFERENCES

Andersen T., 2002. Correction of common lead in U–Pb analyses that do not report 204Pb. Chem. Geol., 192 (2): 59–79. https://doi.org/10.1016/S0009-2541(02)00195-X.

Amelin Y., Lee D.C., Halliday A.N., 2000. The Lu-Hf isotope geochemistry of chondrites and the evolution of the mantle-crust system. Earth Planet. Sci. Lett., 179 (2): 249–262. https://doi.org/10.1016/S0016-7037(00)00493-2.

Baker J., Peate D., Waight T., Meyzen C., 2004. Pb isotopic analysis of standards and samples using a 207Pb–204Pb double spike and thallium to correct for mass bias with a double-focusing mc-icp-ms. Chem. Geol., 211 (3-4): 275–303. https://doi.org/10.1016/j.chemgeo.2004.06.030.

Blichert-Toft J., Chauvel C., Albarède F., 1997. Separation of Hf and Lu for high-precision isotope analysis of rock samples by magnetic sector-multiple collector ICP-MS. Contrib. Mineral. Petrol., 127 (3): 248–260. https://doi.org/10.1007/s004100050278.

Boynton W.V., 1984. Cosmochemistry of the Rare Earth Elements: Meteorite Studies. Rare Earth Elem. Geochem., 2: 63–114. https://doi.org/10.1016/B978-0-444-42148-7.50008-3.

Bouvier A., Vervoort J.D., Patchett P.J., 2008. The Lu-Hf and Sm-Nd isotopic composition of CHUR: Constraints from unequilibrated chondrites and implications for the bulk composition of terrestrial planets. Earth Planet. Sci. Lett., 273 (1-2): 48–57. https://doi.org/10.1016/j.epsl.2008.06.010.

Chen S.S., Fan W.M., Shi R.D., 2021. The Tethyan Himalaya igneous province: Early melting products of the Kerguelen mantle plume. J. Petrol., 62 (1): 1–22. https://doi.org/10.1093/petrology/egab069.

Chen S.S., Fan W.M., Shi R.D., 2018. 118-115 Ma magmatism in the Tethyan Himalaya igneous province: Constraints on Early Cretaceous rifting of the northern margin of Greater India. Earth Planet. Sci. Lett., 491: 21–33. https://doi.org/10.1016/j.epsl.2018.03.034.

Chen Y., Jahn B.M., Wu F.Y., 2020. Post-subduction extensional magmatism in the Central Asian Orogenic Belt: Insights from zircon U-Pb dating and Hf isotopes of the Shama Gabbro. Lithos, 360-361: 105632.

Chayes F., 1956. Petrographic modal analysis. John Wiley and Sons, New York, 113 pp.

Deng J.F., Mo X.X., Zhao H.L., Luo Z.H., Du Y.S., 2004. Petrology of igneous rocks and tectonic environmental evolution. Earth Sci. Front., 11 (2): 217–228. (in Chinese).

Editorial Department of J. Geomech., 2023. Summary of articles on geochronology (2021-2023). J. Geomech., 29 (1): 1–50.

Fisher C.M., 2014. Guidelines for reporting zircon Hf isotopic data by LA-MC-ICPMS and potential pitfalls in the interpretation of these data. Chem. Geol., 363: 125–133. https://doi.org/10.1016/j.chemgeo.2013.10.019.

Fu H., Han J.H., Sun Y.X., 2024. Tethys orogenic belt. Sediment. Geol. Tethyan Geol., 44 (1): 100–133. https://doi.org/10.19826/j.cnki.1009-3850.2023.08008.

Griffin W.L., Pearson N.J., Belousova E., 2000. The Hf isotope composition of cratonic mantle: LAM-ICPMS analysis of zircon megacrysts in kimberlites. Geochim. Cosmochim. Acta, 64 (1): 133–147.

Gao S., Liu Y.S., Hu Z.C., 2008. Lu-Hf isotopic systematics and their applications in petrology. Chin. Sci. Bull., 53 (14): 2091–2110.

Hofmann A.W., 1988. Chemical differentiation of the Earth: The relationship between mantle, continental crust, and oceanic crust. Earth Planet. Sci. Lett., 90 (4): 297–314. https://doi.org/10.1016/0012-821X(88)90132-X.

Hu Z.C., Zhang W., Liu Y.S., Gao S., Li M., Zong K.Q., Chen H.H., Hu S.H., 2015. “Wave” Signal-Smoothing and Mercury-Removing Device for Laser Ablation Quadrupole and Multiple Collector ICPMS Analysis: Application to Lead Isotope Analysis. Anal. Chem., 87 (2): 1152–1157. https://doi.org/10.1021/ac503749k.

Hu Z.C., Liu Y.S., Gao S., Liu W., Yang L., Zhang W., Tong X., Lin L., Zong K.Q., Li M., Chen H., Zhou L., 2012. Improved in situ Hf isotope ratio analysis of zircon using newly designed X skimmer cone and Jet sample cone in combination with the addition of nitrogen by laser ablation multiple collector ICP-MS. J. Anal. At. Spectrom., 27 (9): 1391–1399. https://doi.org/10.1039/c2ja30078h.

Hu X.M., Jansa L., Chen L., 2010. Provenance of Lower Cretaceous Wolong volcaniclastics in the Tibetan Tethyan Himalaya: Implications for the final breakup of eastern Gondwana. Sediment. Geol., 223 (3-4): 193–205. https://doi.org/10.1016/j.sedgeo.2009.11.008.

Hu Z.C., Zhang L.C., Zhao G.C., 2018. Paleoproterozoic crustal evolution of the North China Craton: Constraints from zircon U-Pb-Hf isotopes and whole-rock geochemistry of the Huoqiu iron deposit. Precambrian Res., 312: 244–261.

Humphris S.E., Zierenberg R.A., Mullineaux L.S., Thompson R.E., 1995. Seafloor hydrothermal systems: Physical, chemical, biological, and geological interactions. Geophys. Monogr., 91. https://doi.org/10.1029/GM091.

Irvine T.N., Barager W.R.A., 1971. A guide to the chemical classification of the common volcanic rocks. Can. J. Earth Sci., 8 (5): 523–548. https://doi.org/10.1139/e71-055.

Jin L., Tang S.H., Zhu X.K., Pan C.X., 2017. Production and Certification of the Reference Material GSB 04-3258-2015 as a $^{143}Nd/^{144}Nd$ Isotope Ratio Reference. Geostand. Geoanal. Res., 41 (2): 255–262. https://doi.org/10.1111/ggr.12151.

Jia Z.Q., Hao J.H., Xu Y.L., 2020. Geochemical Characteristics and Genesis of the Volcanic Rocks of the Gangdagai Formation in the Zhongza Massif, Sichuan. Acta Geol. Sichuanica, 40 (4): 686–689.

Jian P., Liu D.Y., Kroner A., 2009. Devonian to Permian plate tectonic cycle of the Paleo-Tethys Orogen in southwest China: Insights from zircon ages of ophiolites, arc/back-arc assemblages and within-plate igneous rocks and generation of the Emeishan CFB province. Lithos, 113 (3-4): 767–784. https://doi.org/10.1016/j.lithos.2009.04.006.

Li C.F., Li X.H., Li Q.L., Guo J.H., Yang Y.H., 2012. Rapid and precise determination of Sr and Nd isotopic ratios in geological samples from the same filament loading by thermal ionization mass spectrometry employing a single-step separation scheme. Anal. Chim. Acta, 727: 54–60. https://doi.org/10.1016/j.aca.2012.03.040.

Lin J., Liu Y.S., Yang Y.H., Hu Z.C., 2016. Calibration and correction of LA-ICP-MS and LA-MC-ICP-MS analyses for element contents and isotopic ratios. Solid Earth Sci., 1 (1): 5–27.

Lu F.X., Sang L.K., 2002. Petrology. Geological Publishing House, Beijing. (in Chinese).

Li C., Zhai Q.G., Dong Y.S., 2006. Formation and evolution of the Tethyan tectonic domain in the Tibetan Plateau. Geol. Bull. China, 25 (1-2): 18–26. (in Chinese).

Li Y., Zhou R.J., Yan Z.K., 2003. Tectonic attribute and evolution of the Zhongza Block in the Sanjiang Orogenic Belt. Chin. J. Geol., 38 (2): 190–201. (in Chinese).

Li T., Rao J.L., 1997. Element Geochemistry. Science Press, Beijing. (in Chinese).

Liu D.Y., Song B., Zhang Z.F., 2003. Zircon U-Pb isotopic dating method and its application. Geol. Bull. China, 22 (12): 917–924. (in Chinese).
Ludwig K.R., 2003. Isoplot 3.00: A Geochronological Toolkit for Microsoft Excel; Special Publication No.4; Berkeley Geochronology Center: Berkeley, CA, USA, pp.1-70.
Liu Y.S., Hu Z.C., Gao S., 2008. In situ analysis of major and trace elements of anhydrous minerals by LA-ICP-MS without applying an internal standard. Chem. Geol., 257 (1-2): 34–43. https://doi.org/10.1016/j.chemgeo.2008.08.004.
Liu Y.S., Gao S., Hu Z.C., Gao C.G., Zong K.Q., Wang D.B., 2010. Continental and oceanic crust recycling-induced melt-peridotite interactions in the Trans-North China Orogen: U-Pb dating, Hf isotopes and trace elements in zircons of mantle xenoliths. J. Petrol., 51 (3): 537–571. https://doi.org/10.1093/petrology/egp082.
Liu Y.S., Hu Z.C., Zong K.Q., 2010. Reappraisement and refinement of zircon U-Pb isotope and trace element analyses by LA-ICP-MS. Chin. Sci. Bull., 55 (15): 1535–1546. https://doi.org/10.1007/s11434-010-3052-4.
Liu J., Zhang Z., Wang Q., 2012. Lithospheric mantle evolution beneath the southern Central Asian Orogenic Belt: Constraints from zircon Hf isotopes of mantle xenoliths. J. Asian Earth Sci., 48: 112–124.
Li Y.D., Tang Y., Wang D.B., 2025. Geochronology, petrogeochemical characteristics and tectonic significance of eclogites in the "Sanyan Area" of the eastern Jinshajiang Suture Zone. J. Geomech., 31 (4): 557–575. https://doi.org/10.12090/j.issn.1006-6616.2025053.
Lu Y.X., Yang J.S., Xu Z.Q., 2022. Possible northward subduction of the Garzê-Litang Ocean: Evidence from magmatic rocks in Daofu-Luhuo, Songpan-Garzê. Acta Geol. Sin., 96 (6): 2380–2402. https://doi.org/10.19762/j.cnki.dizhixuebao.2022123.
Li J., Wang Q., Zhang H.F., 2020. Late Permian magmatism in the western Yangtze Block: Implications for the Emeishan large igneous province. Lithos, 350-351: 105268.
Liu Z.C., Wu F.Y., Ji W.Q., 2014. Petrogenesis of the Ramba leucogranite in the Tethyan Himalaya and constraints on the channel flow model. Lithos, 208-209: 118–136. https://doi.org/10.1016/j.lithos.2014.08.022.
Liu Z., Zhou Q., Lai Y., 2015. Petrogenesis of the Early Cretaceous Laguila bimodal intrusive rocks from the Tethyan Himalaya: Implications for the break-up of Eastern Gondwana. Lithos, 236-237: 190–202. https://doi.org/10.1016/j.lithos.2015.09.006.
Liang J.C., Bian W.W., Jiao X.W., 2023. Geochronological results from the Zhela Formation volcanics of the Tethyan Himalaya and their implications for the breakup of eastern Gondwana. Sci. Rep., 13 (1): 20035. https://doi.org/10.1038/s41598-023-47268-5.
Lv J.S., Xiao Y.F., Deng J.H., Wang T., Cheng C.J., Gong T.T., Yu H.J., Deng Y.B., 2012. Petrochemical characteristics and tectonic setting of the lower Gangdagai Formation in the Xiaozhongdian area, Shangrila. Geol. Explor., 48 (6): 1214–1220.
Le Maitre R.W., 2002. Igneous Rocks: A Classification and Glossary of Terms (2nd ed.). Cambridge Univ. Press, Cambridge.
Metcalfe I., 2013. Gondwana dispersion and Asian accretion: Tectonic and palaeogeographic evolution of eastern Tethys. J. Asian Earth Sci., 66: 1–33. https://doi.org/10.1016/j.jseaes.2012.12.020.
Middlemost E.A.K., 1994. Naming materials in the magma/igneous rock system. Earth-Sci. Rev., 37 (3-4): 215–224. https://doi.org/10.1016/0012-8252(94)90029-9.
Mcdonough W.F., 1990. Constraints on the composition of the continental lithospheric mantle. Earth Planet. Sci. Lett., 101 (1): 1–18. https://doi.org/10.1016/0012-821X(90)90119-I.
Meschede M., 1986. A method of discriminating between different types of mid-ocean ridge basalts and continental tholeiites with the Nb-Zr-Y diagram. Chem. Geol., 56 (3-4): 207–218. https://doi.org/10.1016/0009-2541(86)90004-5.

Muttoni G., Gaetani M., Kent D.V., Sciunnach D., Angiolini L., Berra F., Garzanti E., Mattei M., Zanchi A., 2009. Opening of the Neo-Tethys ocean and the Pangea B to Pangea A transformation during the Permian. GeoArabia, 14 (4): 17–48. https://doi.org/10.2113/geoarabia140417.

Meng F.X., Meng Y.K., Wei Y.Q., 2024. Identification of the EMII-type mantle end-member of the Kerguelen manle plume and its implications for the initial breakup of eastern Gondwana: New constraints from the Cretaceous diabase in the Tethyan Himalaya. J. Asian Earth Sci., 272: 106250. https://doi.org/10.1016/j.jseaes.2024.106250.

McDonough W.F., Sun S.S., 1995. The composition of the Earth. Chem. Geol., 120 (3-4): 223–253. https://doi.org/10.1016/0009-2541(94)00140-4.

Niu Y., O'Hara M.J., 2003. Origin of ocean island basalts: A new perspective from petrology, geochemistry, and mineral physics considerations. J. Geophys. Res.-Solid Earth, 108 (B4): 2209. https://doi.org/10.1029/2002JB002048.

Neal C.R., Mahoney J.J., Chazey W.J., 2002. Mantle sources and the highly variable role of continental lithosphere in basalt petrogenesis of the Kerguelen Plateau and broken ridge LIP: Results from ODP leg 183. J. Petrol., 43 (7): 1177–1205. https://doi.org/10.1093/petrology/43.7.1177.

O'Hara M.J., 1968. Fractional crystallization of a hydrous basalt magma. J. Petrol., 9 (1): 31–83.

Pearce J.A., Cann J.R., 1973. Tectonic setting of basic volcanic rocks determined using trace element analyses. Earth Planet. Sci. Lett., 19 (2): 290–300. https://doi.org/10.1016/0012-821X(73)90135-8.

Pan G.T., Xiao Q.H., Lu S.N., Deng J.F., Feng Y.M., Zhang K.X., 2009. Division of tectonic units of China. Geol. China, 36 (1): 1–28. (in Chinese).

Pearce J., 1982. Trace element characteristics of lavas from destructive plate boundaries. In: R.S. Thorpe (Ed.), Andesites: Orogenic Andesites and Related Rocks. John Wiley and Sons, Chichester, 525–548.

Russell W.A., Papanastassiou D.A., Tombrello T.A., 1978. Ca isotope fractionation on the earth and other solar system materials. Geochim. Cosmochim. Acta, 42 (8): 1075–1090. https://doi.org/10.1016/0016-7037(78)90105-9.

Stern R.J., 2002. Subduction zones. Rev. Geophys., 40 (4): 1-43. https://doi.org/10.1029/2001RG000108.

Shi Y.R., Hou C.Y., Anderson J.L., 2018. Zircon SHRIMP U-Pb age of Late Jurassic OIB-type volcanic rocks from the Tethyan Himalaya: Constraints on the initial activity time of the Kerguelen mantle plume. Acta Geochim., 37 (4): 441–455.

Seton M., Müller R.D., Zahirovic S., Gaina C., Torsvik T., Shephard G., Talsma A., Gurnis M., Turner M., Maus S., Chandler M., 2012. Global continental and ocean-basin reconstructions since 200 Ma. Earth-Sci. Rev., 113 (3-4): 212-270. https://doi.org/10.1016/j.earscirev.2012.03.002.

Steiger R.H., Jager E., 1977. Subcommission on geochronology: Convention on the use of decay constants in geo- and cosmochronology. Earth Planet. Sci. Lett., 36 (3): 359–362. https://doi.org/10.1016/0012-821X(77)90060-7.

Sichuan Bureau of Geology, 1980. Regional Geological Survey Report of the Yidun Sheet (1:200 000). Unpublished internal geological report. Sichuan Bureau of Geology, Chengdu.

Tang Y., Zhai Q.G., 2020. First identification of the MOR-type ophiolites in the Meso-Tethyan suture zone of the Qinghai-Tibet Plateau. GSA Bull., 132 (11-12): 2202–2220. https://doi.org/10.1130/B35500.1.

Taylor S.R., Mclennan S.M., 1985. The continental crust: its composition and evolution. Blackwell Scientific Publications, Oxford.

Tatsumi Y., Eggins S.M., 1995. Genesis of high-Mg andesites and adakites by melting of young lithospheric mantle under garnet amphibolite facies conditions. Earth Planet. Sci. Lett., 134 (1-2): 1–15.

Van Hinsbergen D.J.J., Steinberger B., Doubrovine P.V., 2011. Acceleration and deceleration of India-Asia convergence since the Cretaceous: Roles of mantle plumes and continental collision. J. Geophys. Res.-Solid Earth, 116 (B6): 1-20. https://doi.org/10.1029/2010JB008051.
Wilson M., 1989. Igneous Petrogenesis: A Global Tectonic Approach. Unwin Hyman, London.
Woodhead J., Hergt J., Shelley M., Eggins S., Kemp R., 2004. Zircon Hf-isotope analysis with an excimer laser, depth profiling, ablation of complex geometries, and concomitant age estimation. Chem. Geol., 209 (3-4): 121–135. https://doi.org/10.1016/j.chemgeo.2004.04.026.
Wilson M., 2007. Igneous Petrogenesis: A Global Tectonic Approach. Springer, Dordrecht.
Winter J.D., 2014. An Introduction to Igneous and Metamorphic Petrology (4th edn). Pearson, New York.
Wang E.Q., Yang J.S., Xu Z.Q., 2007. Meso-Cenozoic tectonic evolution of the eastern Tethyan tectonic domain. Acta Geol. Sin.-Engl. Ed., 81 (8): 1305–1320.
Wang Y.J., 2024. Paleo-Tethyan magmatism in the Jinshajiang-Ailaoshan-Mojiang tectonic belt. Sci. Press, Beijing.
Winchester J.A., Floyd P.A., 1977. Geochemical discrimination of different magma series and their differentiation products using immobile elements. Chem. Geol., 20 (4): 325–343. https://doi.org/10.1016/0009-2541(77)90057-2.
Wood D.A., 1980. The application of a Th-Hf-Ta diagram to problems of tectonomagmatic classification and to establishing the nature of crustal contamination of basaltic lavas of the British Tertiary Volcanic Province. Earth Planet. Sci. Lett., 50 (1): 11–30. https://doi.org/10.1016/0012-821X(80)90116-8.
Wang D.B., Wang B.D., Tang Y., Luo L., He J., Jiang L.L., Zhao H.S., Chen L., 2021. Research progress and prospects of Tethys in Sanjiang orogenic belt, Southwest China. Geol. Bull. China, 40 (12): 1799–1813.
Wang L.Q., Pan G.T., Li D.M., 1999. The Spatio-temporal Framework and Geological Evolution of the Jinsha jiang Arc-Basin Systems. Acta Geol. Sin., 73 (2): 206–218.
Wang B.D., Wang L.Q., Wang D.B., 2021. The temporal and spatial framework and its tectonic evolution of the Jinsha River arc-basin system, Southwest China. Sediment. Geol. Tethyan Geol., 41 (2): 246–264.
Wu F.Y., Wan B., Zhao L., Xiao W.J., Zhu R.X., 2020. Tethyan geodynamics. Acta Petrol. Sin., 36 (6): 1627–1674. https://doi.org/10.18654/1000-0569/2020.06.01.
Wang T., Hu Y., Guo D.J., Ling Y.J., Wang Q., 2022. Pterogeochemistry of Volcanic Rock of the Upper Permian Gangdagai Formation in the Waka Town-Gangxue Zone, Derong. Acta Geol. Sichuan., 42 (1): 117–122.
Yang T.S., Ma Y.M., Bian W.W., 2015. Paleomagnetic results from the Early Cretaceous Lakang Formation lavas: Constraints on the paleo-latitude of the Tethyan Himalaya and the India-Asia collision. Earth Planet. Sci. Lett., 428: 120–133. https://doi.org/10.1016/j.epsl.2015.07.037.
Yoshida M., 2014. Effects of various lithospheric yield stresses and different mantle-heating modes on the breakup of the Pangea supercontinent. Geophys. Res. Lett., 41 (9): 3060-3067. https://doi.org/10.1002/2014GL060023.
Yin A., Harrison T.M., 2000. Geologic evolution of the Himalayan-Tibetan orogeny. Annu. Rev. Earth Planet. Sci., 28: 211–280. https://doi.org/10.1146/annurev.earth.28.1.211.
Zhong D.L., Ding L., 1996. Tectonic development of the Tibetan Plateau. Sci. China Ser. D, 26 (4): 289–295. (in Chinese).
Zhang J.X., Meng F.C., Yu S.Y., 2008. Coupling relationship between the Jinshajiang Suture Zone and tectonic evolution of the Zhongza Block. Acta Petrol. Sin., 24 (9): 2027–2038. (in Chinese).
Zhu D.C., Mo X.X., Dong G.C., 2009. Middle Triassic magmatism in the Sanjiang Orogenic Belt and closure of the Paleo-Tethys Ocean. Earth Sci.-J. China Univ. Geosci., 34 (4): 721–732. (in Chinese).
Zhou X.R., Zhao Z.H., 1989. Principles and applications of trace element geochemistry. Geological Publishing House, Beijing. (in Chinese).

Zheng Y.F., Chen J.F., 2000. Isotope Geochemistry. Science Press, Beijing. (in Chinese).
Zhang W., Hu Z.C., 2020. Estimation of isotopic reference values for pure materials and geological reference materials. At. Spectrosc., 41 (3): 93–102.
Zhang W., Hu Z.C., Liu Y.S., 2020. Iso-Compass: new freeware software for isotopic data reduction of LA-MC-ICP-MS. J. Anal. At. Spectrom., 35 (5): 1087–1096. https://doi.org/10.1039/D0JA00034A.
Zindler A., Hart S.R., 1986. Chemical geodynamics. Annu. Rev. Earth Planet. Sci., 14: 493–571. https://doi.org/10.1146/annurev.ea.14.050186.002425.
Zhu D.C., Mo X.X., Pan G.T., 2008. Petrogenesis of the earliest Early Cretaceous mafic rocks from the Cona area of the eastern Tethyan Himalaya in south Tibet: Interaction between the incubating Kerguelen plume and the eastern Greater India lithosphere. Lithos, 100 (1-4): 147–173. https://doi.org/10.1016/j.lithos.2007.06.024.
Zhou Q., Liu Z., Lai Y., 2018. Petrogenesis of mafic and felsic rocks from the Comei large igneous province, South Tibet Implications for the initial activity of the Kerguelen plume. GSA Bull., 130 (5-6): 811–824. https://doi.org/10.1130/B31653.1.
Zhang K.X., He W.H., Xu Y.D., 2021. Reconstruction of main types for oceanic plate strata in the subduction-accretionary complex and feature of sequence for each type: an example from the Qinghai-Tibet Tethyan Permian strata. Sediment. Geol. Tethyan Geol., 41 (2): 137–151. (in Chinese with English abstract).
Zeng Y.C., Xu J.F., Chen J.L., 2019. Breakup of Eastern Gondwana as inferred from the Lower Cretaceous Charong Dolerites in the central Tethyan Himalaya, southern Tibet. Palaeogeogr. Palaeoclimatol. Palaeoecol., 517: 70–82. https://doi.org/10.1016/j.palaeo.2018.08.014.
Zhang Z., Li G.M., He X.Z., 2023. The evolution of Kerguelen mantle plume and breakup of eastern Gondwana: New insights from multistage Cretaceous magmatism in the Tethyan Himalaya. Gondwana Res., 119: 68–85. https://doi.org/10.1016/j.gr.2023.03.009.

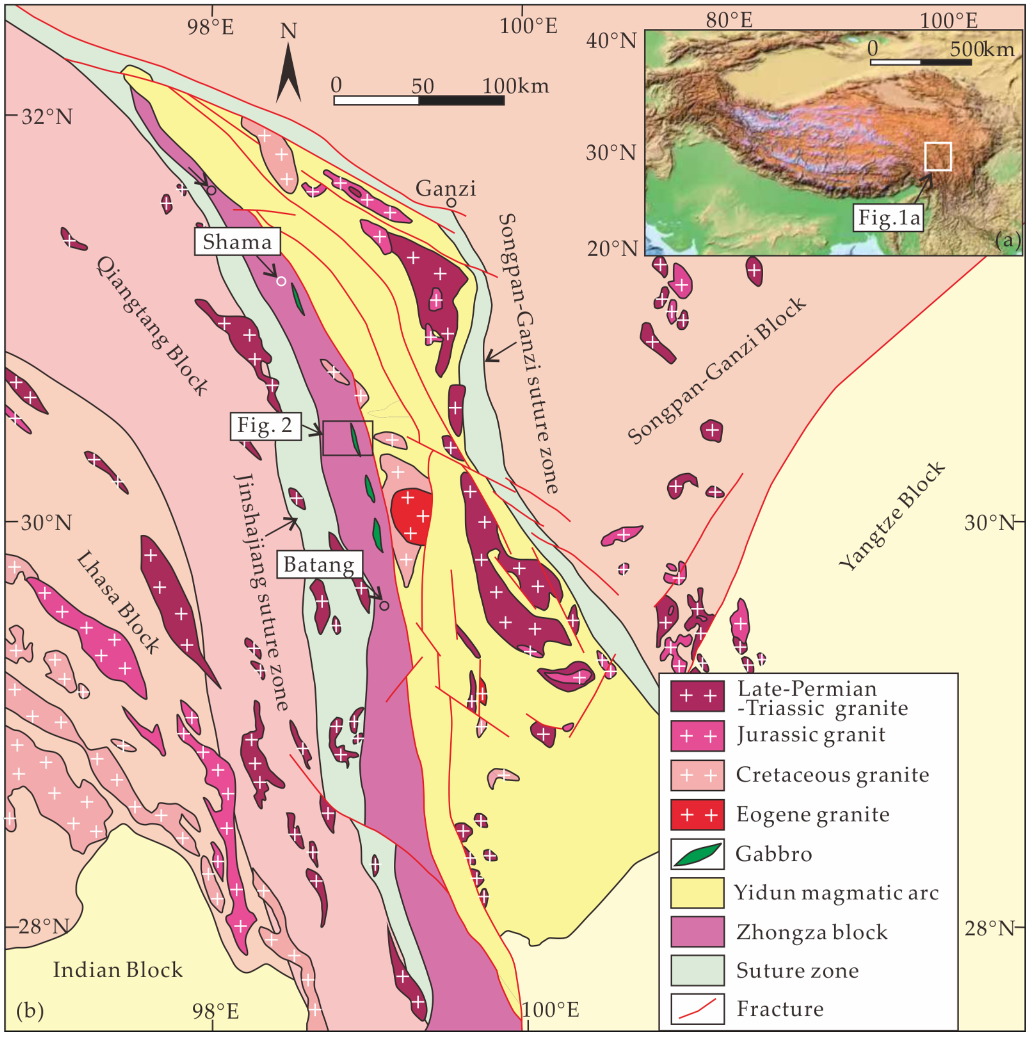

Figure 1. Tectonic subdivision of the eastern Paleo-Tethyan orogenic belt and location of the study area (revised after Hou *et al*., 2003).

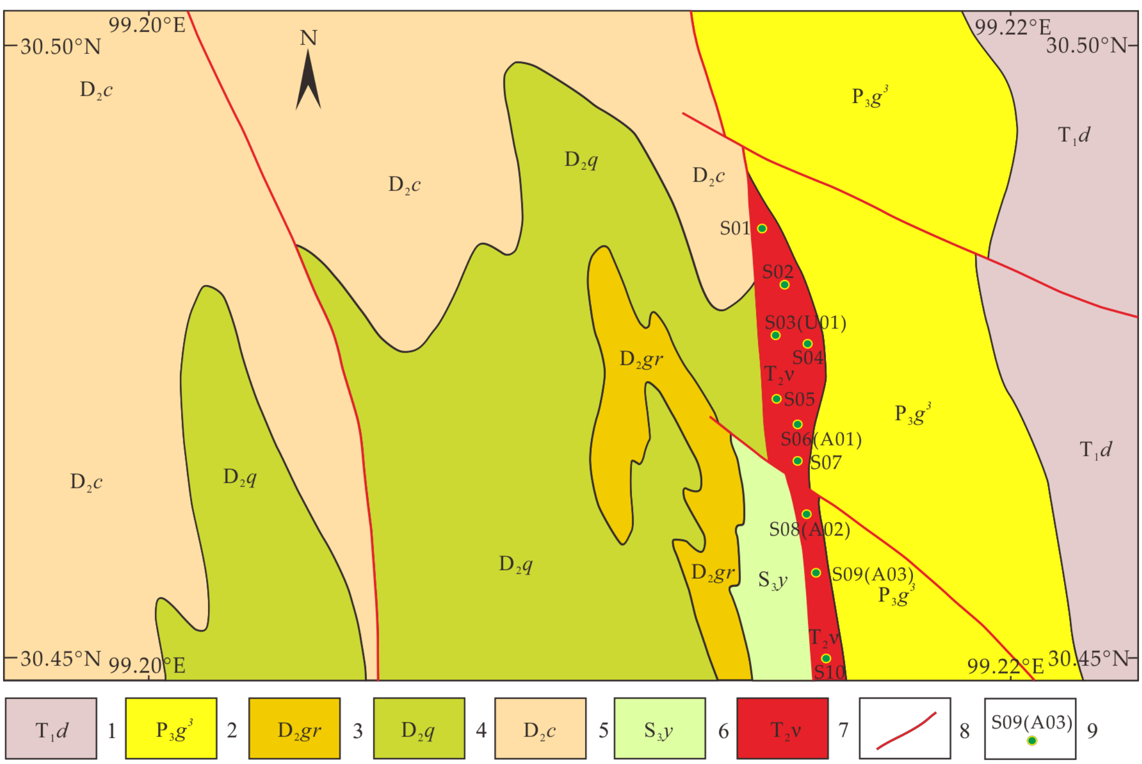

Figure 2. Geological map of the Shama gabbro. 1.Early Triassic Dang'en Formation; 2. Late Permian Gangdagai Formation; 3. Middle Devonian Gerong Formation; 4. Middle Devonian Qujing Formation; 5. Middle Devonian Cangna Formation; 6. Late Silurian Yongren Formation; 7. Middle Triassic gabbro; 8. Fault; 9. Sampling locations.

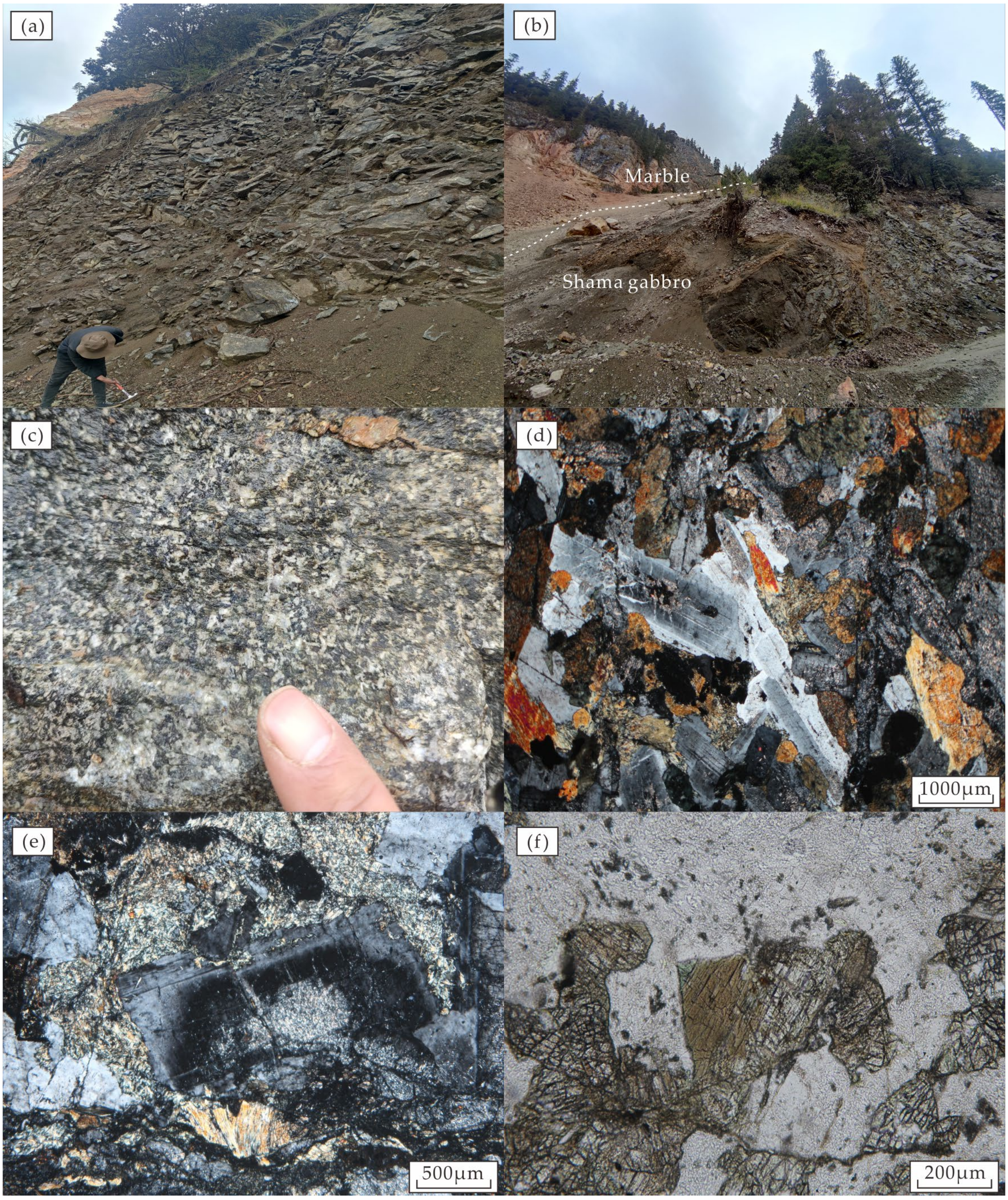

Figure 3. Field and microscopic photographs of the Shama gabbro. (a,b,c) field photos of the Shama gabbro; (d) Gabbroic texture; (e) Plagioclase zoning texture; (f) Pyroxene with amphibole reaction rim.

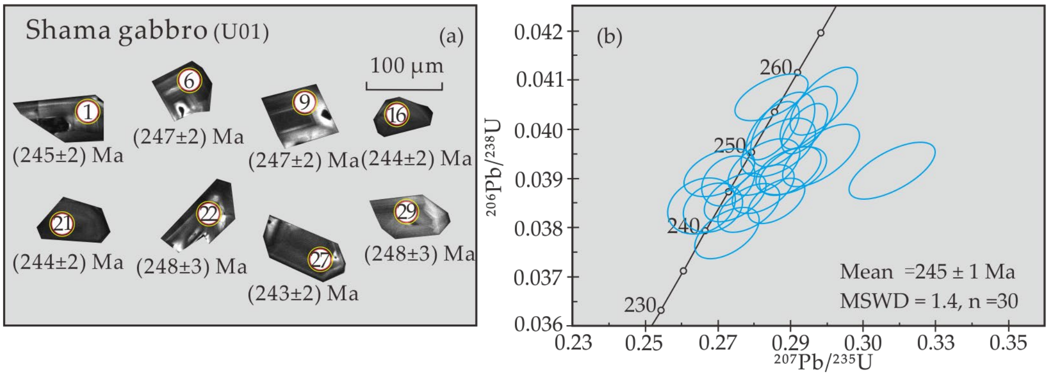

Figure 4. Cathodoluminescence (CL) images of representative zircon grains (a) and concordiaplots (b) of zircon from Shama gabbro. Red circles indicate locations of LA-ICPMS U-Pb dating, while big yellow circles indicate LA-MC-ICPMS Hf isotope analyses positions

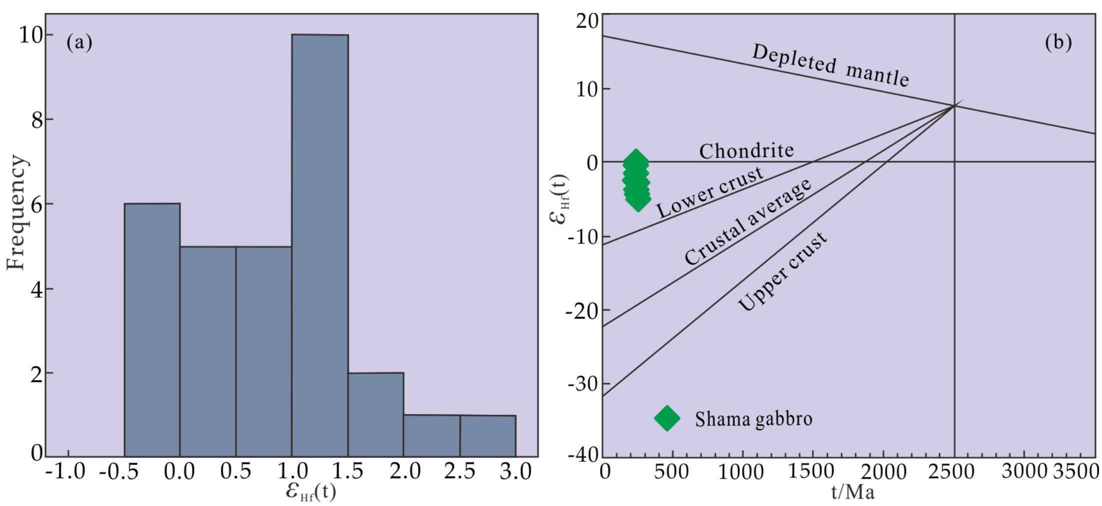

Figure 5. Diagram of frequency histograms of ε_{Hf}(t) (a) and t vs. ε_{Hf}(t) (b) of zircons for Shama gabbro

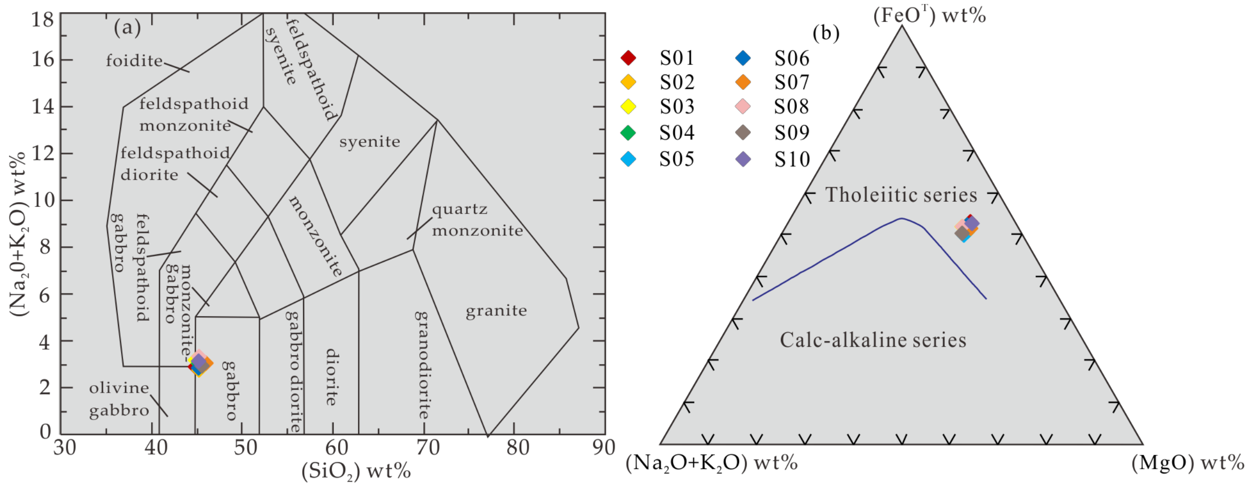

Figure 6. ($K_2O + Na_2O$) wt% versus (SiO_2) wt% (a) and (K_2O+Na_2O) wt% versus (MgO) wt% versus (FeO^T) wt% (b) diagram of Shama gabbro ((a) after E.A.K.Middlemost, 1994; (b) after Irvine T. N. *et al*., 1971). Th- Tholeiitic basalt series, Ca- calc-alkaline series

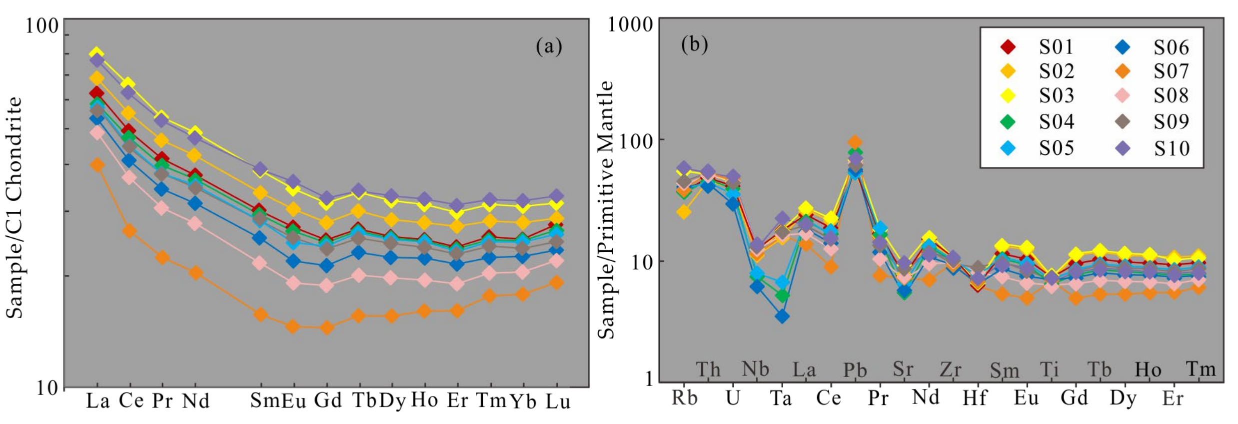

Figure 7. (a) Chondrite-normalized REE distribution patterns (after Boynton, 1984) and (b) Primitive mantle-normalized trace elements distribution patterns (after Sun and Mc Donough, 1989) for the Shama gabbro

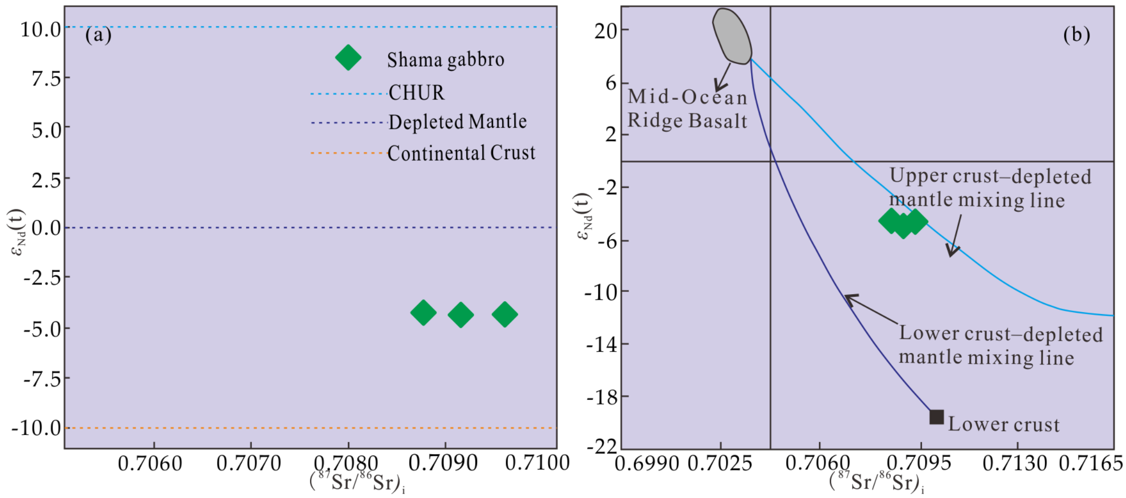

Figure 8. Diagram of ε_{Nd}(t) vs. $(^{87}Sr/^{86}Sr)_i$ for Shama gabbro ((a) and (b) after Bouvier A *et al*., 2008)

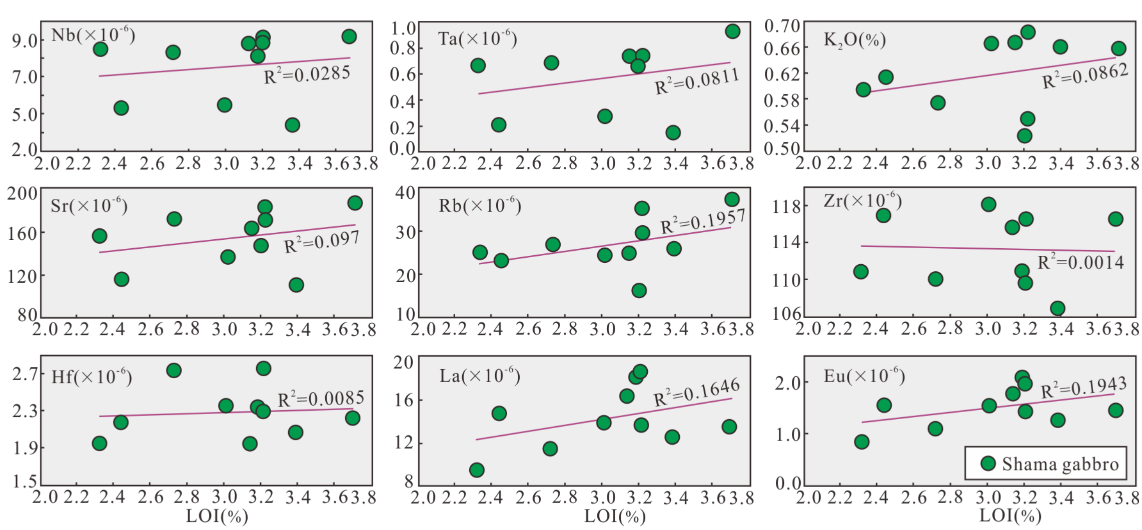

Figure 9. The diagrams of whole-rock elements and isotopes vs. LOI (loss on ignition) for the Shama gabbro

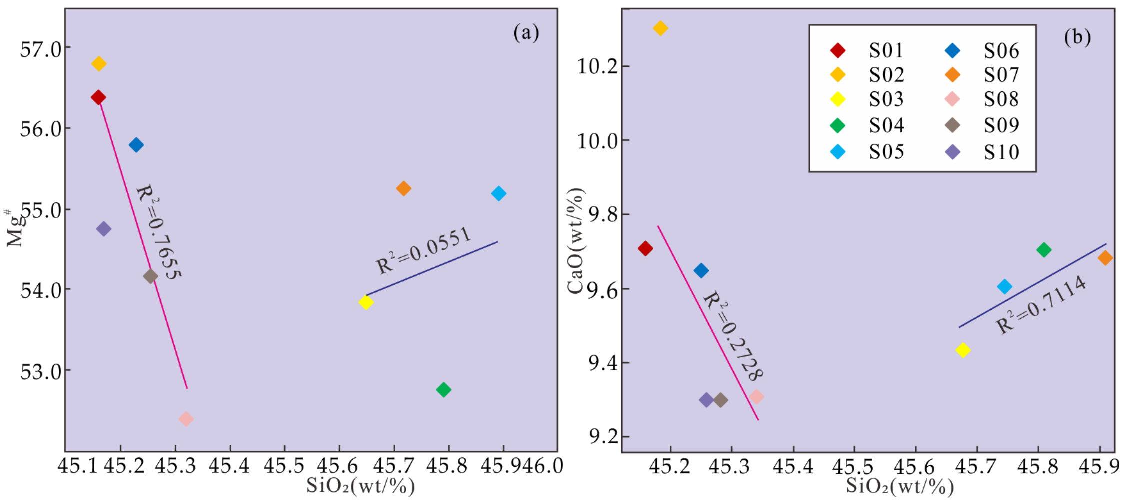

Figure 10. $Mg^{\#}$ vs.SiO_2 (a) and CaO vs.SiO_2 (b) for Shama gabbro

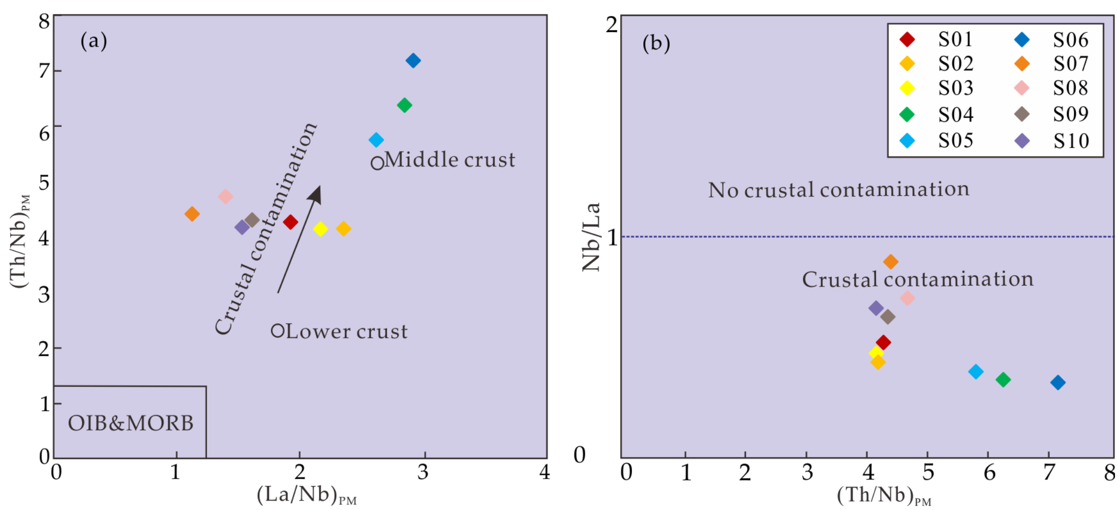

Figure 11. Discrimination diagrams of $(La/Nb)_{PM}$ vs.$(Th/Nb)_{PM}$ (a) and $(Th/Nb)_{PM}$ vs.Nb/La (b) for Shama gabbro ((a) and (b) after Neal CR *et al*., 2002)

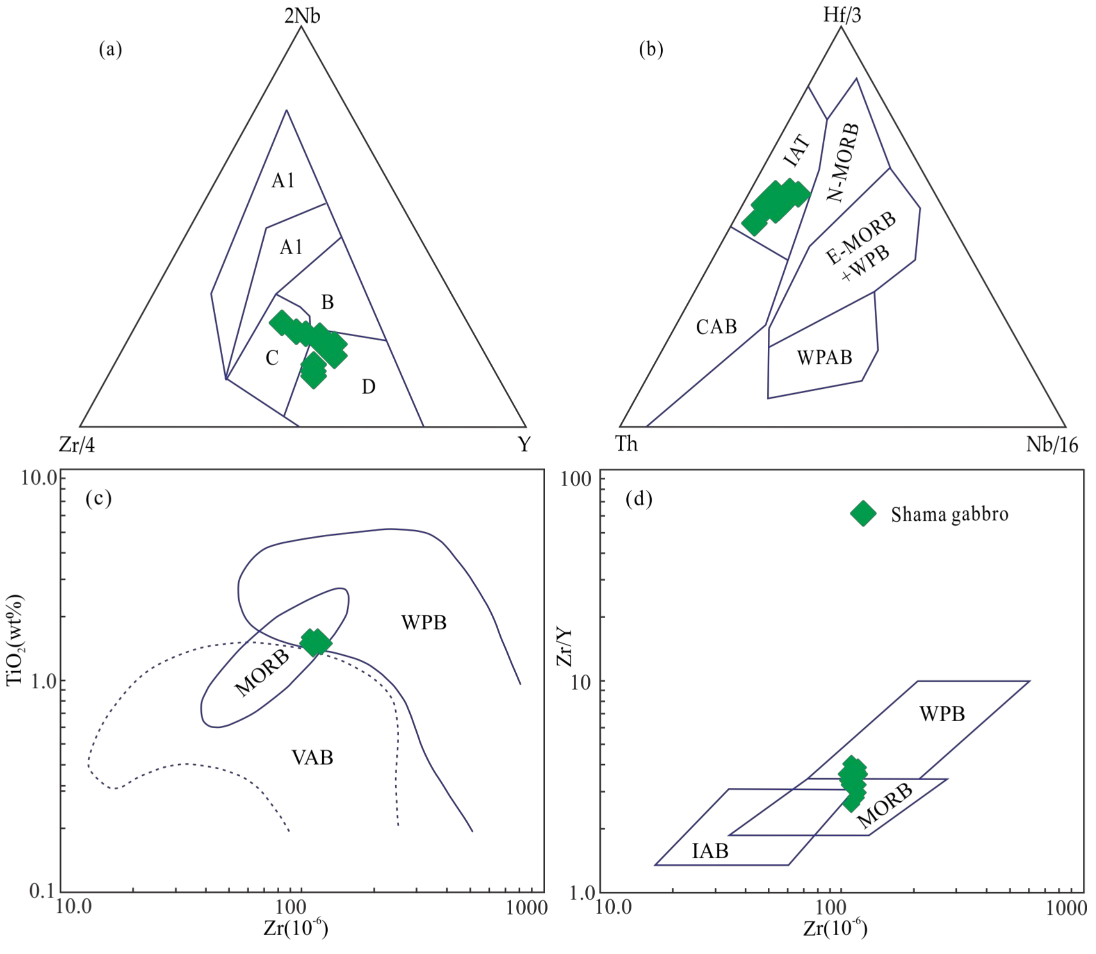

Figure 12. 2Nb-Zr/4-Y (a), Hf/3-Th-Nb/16 (b) TiO_2 vs. Zr (c), Zr/Y vs.Zr (d) diagrams for Shama gabbro (a.after Meschede, 1986; b. after Wood DA, 1980; c. after Pearce J, 1982; d. after Pearce, 1996). A1- Intraplate Alkaline Basalt；A2- Intraplate Alkaline Basalt and Tholeiitic Basalt；B-Plume-Ridge Basalt；C- Intraplate Tholeiitic Basalt and Volcanic Arc Basalt；D-Volcanic Arc Basalt and Normal Mid-Ocean Ridge Basalt；IAT-Island Arc Tholeiitic Basalt；CAB- Island Arc Calc-alkaline Basalt；IAB-Island Arc Basalt；MORB-Mid-Ocean Ridge Basalt；N-MORB- Normal Mid-Ocean Ridge Basalt；E-MORB- Enriched Mid-Ocean Ridge Basalt ; WPB- Intraplate Basalt; WPAB- Intraplate Alkaline Basalt; OIB- Ocean Island Basalt；BBAB- Back-arc Basin Basalt

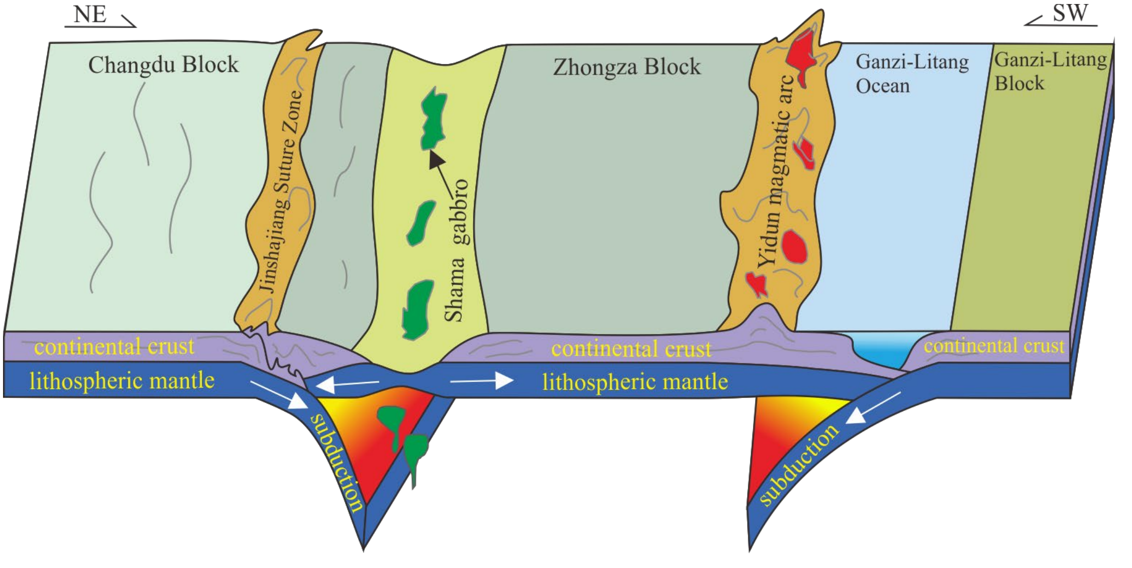

Figure 13. Schematic tectonic evolution model of the Zhongza Block during the Early–Middle Triassic

Table 1. LA - ICP - MS Zircon U - Pb age of the Shama gabbro

Spot	**Content (×10^{-6})**			**Isotope Ratio**							**Age (Ma)**					
U01	**Pb**	**Th**	**U**	**^{207}Pb/^{206}Pb**	**1σ**	**^{207}Pb/^{235}U**	**1σ**	**^{206}Pb/^{238}U**	**1σ**	**Th/U**	**^{207}Pb/^{206}Pb**	**1σ**	**^{207}Pb/^{235}U**	**1σ**	**^{206}Pb/^{238}U**	**1σ**
1	34.9	646	476	0.0521	0.0012	0.2774	0.0058	0.0387	0.0004	1.3554	287	50	249	5	245	2
2	45	877	553	0.0534	0.0009	0.2878	0.0047	0.0391	0.0003	1.5863	346	41	257	4	247	2
3	29.5	522	426	0.0506	0.0011	0.2684	0.0056	0.0385	0.0003	1.2261	233.4	51.8	241	4	243	2
4	36.5	621	519	0.0542	0.0012	0.2912	0.0058	0.039	0.0004	1.1963	376	53	260	5	247	2
5	43	793	542	0.054	0.0011	0.2944	0.006	0.0395	0.0004	1.4636	372	44	262	5	250	2
6	49.1	892	676	0.0539	0.001	0.2904	0.0051	0.0391	0.0004	1.3197	369	41	259	4	247	2
7	78.4	1518	925	0.052	0.0008	0.2871	0.0052	0.0401	0.0005	1.6417	283	32	256	4	253	3
8	115	2371	1272	0.0518	0.0009	0.2853	0.0046	0.04	0.0004	1.8632	280	39	255	4	253	2
9	38.1	699	512	0.052	0.0012	0.2798	0.0063	0.0391	0.0004	1.3655	287	54	250	5	247	2
10	79.7	1354	1181	0.0533	0.0008	0.2944	0.0045	0.04	0.0003	1.1468	343	35	262	4	253	2
11	32.3	544	433	0.0538	0.0014	0.2997	0.0063	0.0406	0.0004	1.2549	361	57	266	5	257	3
12	34	579	463	0.0509	0.0012	0.2852	0.0066	0.0406	0.0003	1.25	235	49	255	5	257	2
13	20.5	357	300	0.0549	0.0013	0.2986	0.007	0.0394	0.0004	1.1908	409	47	265	5	249	3
14	78.2	1462	1072	0.0532	0.0008	0.2826	0.0038	0.0386	0.0004	1.3631	345	35	253	3	244	2
15	61.8	1207	781	0.0506	0.0009	0.2719	0.005	0.0389	0.0004	1.5443	233	41	244	4	246	2
16	32.1	485	551	0.0539	0.001	0.2863	0.0051	0.0386	0.0003	0.8796	365	43	256	4	244	2
17	34.4	593	501	0.0528	0.001	0.2816	0.0049	0.0387	0.0003	1.1826	317	45	252	4	245	2
18	44.6	872	561	0.0529	0.001	0.2823	0.0051	0.0387	0.0003	1.554	324	41	252	4	245	2
19	46.7	916	615	0.0514	0.001	0.2692	0.0052	0.0381	0.0004	1.4896	257	46	242	4	241	2
20	45.9	875	590	0.0522	0.0012	0.2763	0.0066	0.0383	0.0004	1.4838	295	52	248	5	243	2
21	57.7	1127	699	0.0527	0.001	0.2795	0.0052	0.0385	0.0003	1.6131	317	47	250	4	244	2
22	26.1	442	340	0.059	0.0015	0.3183	0.0081	0.0392	0.0004	1.3002	569	49	281	6	248	3
23	29.1	545	394	0.0503	0.0014	0.266	0.0068	0.0385	0.0004	1.3829	209	63	239	5	243	2
24	96	1989	1113	0.0513	0.0007	0.2731	0.0044	0.0386	0.0003	1.788	254	31	245	4	244	2
25	39.1	723	484	0.0526	0.001	0.2876	0.0061	0.0396	0.0004	1.495	322	17	257	5	250	2
26	25.4	483	358	0.0522	0.0012	0.2728	0.0061	0.0379	0.0003	1.3487	295	52	245	5	240	2
27	35.8	679	497	0.0525	0.001	0.2785	0.0056	0.0384	0.0004	1.3661	309	44	249	4	243	2
28	35.2	580	503	0.0533	0.0011	0.2951	0.0054	0.0403	0.0004	1.1542	343	44	263	4	254	3
29	16.3	278	231	0.0522	0.0014	0.2815	0.007	0.0392	0.0004	1.2052	295	59	252	6	248	3
30	32.4	603	438	0.0501	0.0011	0.27	0.0059	0.0391	0.0003	1.3766	198	52	243	5	247	2

Table 2. LA-ICP-MS zircon In Situ Hf Isotopic date of the Shama gabbro

point	age (Ma)	$^{176}Yb/^{177}Hf$	$^{176}Lu/^{177}Hf$	$^{176}Hf/^{177}Hf$	±2σ	$\varepsilon_{Hf}(0)$	$\varepsilon_{Hf}(t)$	$t_{DM1}(Hf)$	$t_{DM2}(Hf)$	$f_{Lu/Hf}$
1	245	0.107866	0.002208	0.282678	0.000021	-3.3	1.68	840	1002	-0.93
2	247	0.104422	0.002284	0.282708	0.000019	-2.2	2.81	797	945	-0.93
3	243	0.065788	0.00153	0.282627	0.000014	-5.1	-0.03	898	1091	-0.95
4	247	0.066609	0.001566	0.282629	0.000015	-5	0.13	895	1085	-0.95
5	250	0.116192	0.002482	0.282667	0.000014	-3.7	1.37	862	1023	-0.93
6	247	0.106657	0.002563	0.28268	0.000019	-3.2	1.77	845	999	-0.92
7	253	0.066854	0.001459	0.28266	0.000012	-4	1.35	849	1026	-0.96
8	253	0.092427	0.001968	0.28264	0.000015	-4.7	0.55	889	1068	-0.94
9	247	0.071027	0.001577	0.28266	0.000013	-4	1.2	852	1030	-0.95
10	253	0.079747	0.001855	0.282639	0.000012	-4.7	0.56	888	1068	-0.94
11	257	0.112151	0.002412	0.282663	0.000017	-3.9	1.37	867	1028	-0.93
12	257	0.085436	0.001859	0.282608	0.000013	-5.8	-0.46	932	1124	-0.94
13	249	0.05528	0.001234	0.282611	0.000016	-5.7	-0.43	914	1117	-0.96
14	244	0.104268	0.002121	0.28264	0.000015	-4.7	0.36	893	1071	-0.94
15	246	0.105538	0.002281	0.282692	0.000014	-2.8	2.2	821	976	-0.93
16	244	0.07791	0.001844	0.282652	0.000012	-4.3	0.8	870	1048	-0.94
17	245	0.093112	0.002191	0.282624	0.000015	-5.2	-0.22	919	1102	-0.93
18	245	0.117595	0.002523	0.282632	0.000016	-4.9	0.04	914	1088	-0.92
19	241	0.112275	0.002479	0.282667	0.000016	-3.7	1.2	862	1024	-0.93
20	243	0.102579	0.002255	0.282669	0.000012	-3.6	1.34	854	1018	-0.93
21	244	0.074354	0.001671	0.282634	0.000014	-4.9	0.2	891	1079	-0.95
22	248	0.074708	0.001665	0.282638	0.000013	-4.8	0.42	885	1071	-0.95
23	243	0.130193	0.002824	0.282665	0.000015	-3.8	1.1	874	1031	-0.91
24	244	0.127949	0.002709	0.282671	0.000014	-3.6	1.37	861	1018	-0.92
25	250	0.118491	0.002846	0.28263	0.000026	-5	-0.01	927	1095	-0.91
26	240	0.088379	0.00198	0.282658	0.000013	-4	0.91	864	1039	-0.94
27	243	0.098707	0.002164	0.282658	0.000016	-4	0.97	868	1038	-0.93
28	254	0.061418	0.001369	0.282657	0.00001	-4.1	1.3	851	1030	-0.96
29	248	0.087382	0.001852	0.282616	0.00002	-5.5	-0.37	921	1112	-0.94
30	247	0.092327	0.001943	0.282656	0.000014	-4.1	1.03	865	1038	-0.94

Table 3. Contents of major elements (wt. %), trace elements (ppm), CIPW-norm of the Shama gabbro

Sample	S01	S02	S03	S04	S05	S06	S07	S08	S09	S10
SiO_2	45.2	45.2	45.7	45.8	45.9	45.2	45.7	45.3	45.2	45.3
TiO_2	1.54	1.49	1.55	1.5	1.47	1.48	1.48	1.43	1.54	1.49
Al_2O_3	14.6	15.1	15.1	15.5	14.6	14.6	15.2	14.9	13.7	15.1
Fe_2O_3	2	2.05	1.42	0.37	1.82	1.44	2.61	0.04	2.28	1.62
FeO	10.1	9.5	10.5	11.4	10.5	10.5	9.9	12.4	11.2	10.5
MnO	0.17	0.17	0.18	0.18	0.17	0.16	0.18	0.18	0.19	0.18
MgO	9.01	8.66	8.24	8.31	8.82	8.98	8.56	8.79	9.33	8.38
CaO	9.7	10.3	9.44	9.69	9.67	9.65	9.6	9.31	9.21	9.3
Na_2O	1.97	2.19	2.02	2.05	2	1.88	1.94	1.89	1.69	1.96
K_2O	0.67	0.52	0.68	0.61	0.67	0.66	0.59	0.57	0.55	0.65
P_2O_5	0.23	0.23	0.24	0.23	0.22	0.22	0.22	0.23	0.23	0.23
LOI	3.13	3.18	3.2	2.44	3	3.37	2.32	2.72	3.2	3.68
Total	98.33	98.56	98.16	98.03	98.82	98.23	98.22	97.72	98.27	98.29
FeO^T	11.9	11.4	11.7	11.7	12.1	11.8	12.2	12.4	13.2	11.9
$Mg^\#$	56.4	56.8	53.8	52.8	55.2	55.8	55.2	52.4	54.8	54.1
Anorthite (An)	30.6	31.3	31.6	32.6	30.3	31.1	32.2	32	29.7	32.1
Albite (Ab)	17.5	19.4	18	18.1	17.6	16.7	17.1	16.8	15	17.5
K-feldspar (Fk)	4.15	3.25	4.25	3.8	4.11	4.12	3.65	3.56	3.43	4.09
Diopside (Di)	15	16.9	13.2	13.3	15	14.6	13	12.4	13.7	12.4
Hypersthene (Hy)	11	6.08	14.2	10.6	13.2	12.5	16.7	12.4	20.2	14.8
Olivine (Ol)	17.1	18.4	14.5	19.3	15.4	17.1	11.3	21	12.2	14.7
Ilmenite (Il)	3.07	2.96	3.09	2.98	2.91	2.95	2.93	2.86	3.08	2.99
Magnetite (Mt)	3.04	3.12	2.17	0.56	2.76	2.2	3.95	0.06	3.47	2.48
Apatite (Ap)	0.57	0.56	0.59	0.55	0.54	0.53	0.53	0.55	0.55	0.55
Alkali Feldspar (A)	5.26	4.2	5.39	4.79	5.23	5.16	4.57	4.45	4.24	5.13
Plagioclase (Pl)	53.4	55.8	54.7	54.6	52.8	52.5	55	52.1	49.6	54.7
Plagioclase Feldspar Grade (An%)	62.3	60.3	62.3	62.9	61.8	63.6	63.9	64.2	65.1	63.4
Differentiation Index (DI)	21.7	22.7	22.3	22	21.7	20.9	20.8	20.4	18.5	21.6
Mg'	0.67	0.68	0.63	0.6	0.65	0.65	0.67	0.58	0.65	0.64
A/NK	3.7	3.62	3.71	3.83	3.66	3.84	3.95	3.99	4.07	3.84
A/CNK	0.7	0.68	0.73	0.73	0.7	0.7	0.73	0.74	0.7	0.74
R1	2167	2116	2197	2230	2201	2231	2205	2290	2297	2206
R2	1862	1917	1806	1833	1836	1860	1824	1815	1807	1804
A/MF	0.58	0.62	0.67	0.72	0.59	0.6	0.61	0.67	0.52	0.65
C/MF	0.7	0.76	0.76	0.82	0.71	0.71	0.7	0.76	0.63	0.73
Sc	44.7	44.7	47.4	31.8	37.8	33.4	47	48.5	54.2	50.9
Ga	22.5	21.4	24.4	17.5	18.3	16.5	24	23.4	23.8	24.4
Rb	24.7	16.1	35.4	23.3	24.8	26.1	25	26.8	29.4	37.1
Sr	163	146	183	117	137	111	156	172	171	188
Y	37.6	41.8	41.1	32.7	32.9	29.5	22.4	26.2	33.6	31.8
Zr	116	111	116	118	118	107	111	110	110	117
Nb	8.82	8.05	9	5.29	5.51	4.41	8.5	8.34	8.78	9.19
Hf	1.95	2.32	2.29	2.18	2.35	2.07	1.96	2.74	2.77	2.23
Ta	0.73	0.64	0.73	0.22	0.28	0.15	0.67	0.68	0.72	0.93
Th	4.48	4	4.45	3.93	3.77	3.73	4.44	4.65	4.53	4.54
U	0.95	0.88	1.05	0.84	0.75	0.62	0.96	1.01	0.96	1.03
La	16.5	18.3	18.9	14.7	14	12.7	9.56	11.6	13.6	13.5
Ce	33.7	37.6	38.5	29.9	28.9	25.1	16.3	22.6	27.5	27.1
Pr	4.42	5	5.1	3.93	3.8	3.26	2.14	2.9	3.61	3.58
Nd	19.7	22.2	22.7	17.4	17.1	14.6	9.55	13	16.4	16.3
Sm	5.14	5.92	5.88	4.59	4.48	3.86	2.41	3.3	4.32	4.3
Eu	1.75	2.08	2	1.57	1.53	1.27	0.85	1.11	1.42	1.47
Gd	5.73	6.64	6.47	5.13	5.09	4.38	2.98	3.88	4.94	4.87
Tb	1.12	1.27	1.26	0.99	1	0.87	0.58	0.75	0.99	0.95
Dy	7.22	8.34	8.11	6.47	6.53	5.69	3.96	5	6.38	6.24
Ho	1.58	1.82	1.77	1.41	1.4	1.27	0.91	1.1	1.41	1.35
Er	4.5	5.15	4.92	3.95	3.96	3.56	2.67	3.15	3.87	3.8
Tm	0.72	0.82	0.79	0.64	0.65	0.57	0.45	0.52	0.65	0.61
Yb	4.73	5.43	5.23	4.19	4.27	3.84	3.04	3.48	4.25	4.04
Lu	0.73	0.83	0.8	0.7	0.66	0.6	0.49	0.56	0.68	0.63
ΣREE	107.6	121.4	122.4	95.6	93.3	81.6	55.9	72.9	90.1	88.8
LREE	81.2	91.1	93.1	72.1	69.7	60.8	40.8	54.5	66.9	66.3
HREE	26.3	30.3	29.4	23.5	23.6	20.8	15.1	18.4	23.2	22.5
LREE/HREE	3.09	3.01	3.17	3.07	2.96	2.93	2.71	2.95	2.89	2.95
$(La/Yb)_N$	2.5	2.42	2.59	2.51	2.35	2.37	2.26	2.39	2.3	2.41
δEu	0.99	1.02	0.99	0.99	0.98	0.94	0.97	0.95	0.94	0.98
δCe	0.97	0.96	0.96	0.97	0.97	0.96	0.89	0.95	0.96	0.95
$(Th/Nb)_{PM}$	4.26	4.17	4.15	6.23	5.74	7.09	4.38	4.68	4.33	4.14
$(La/Nb)_{PM}$	1.94	2.36	2.18	2.88	2.64	2.99	1.17	1.44	1.61	1.52
Nb/La	0.53	0.44	0.48	0.36	0.39	0.35	0.89	0.72	0.65	0.68
La/Sm	3.21	3.09	3.21	3.2	3.13	3.29	3.97	3.52	3.15	3.14

Table 4. Whole-rock Sr-Nd isotope results for the Shama gabbro

	Sample	Age(Ma)	$^{87}Rb/^{86}Sr$	$^{87}Sr/^{86}Sr$	$(^{87}Sr/^{86}Sr)_i$	2SE	$^{147}Sm/^{144}Nd$	$^{143}Nd/^{144}Nd$
Shama gabbro	A01	245	0.44	0.711091	0.709559	0.000005	0.1574	0.512358
	A02	245	0.318	0.710355	0.709247	0.000009	0.1614	0.512361
	A03	245	0.559	0.71065	0.7087	0.00001	0.1564	0.512356

$\varepsilon_{Nd}(t)$	t_{DM2}(Ga)
-4.24	1.36
-4.3	1.36
-4.24	1.36